Seismic Hazard Screening (SHS): Fault Reactivation

Version 1.1

Authors
Paul van den Hoek
Jorik Poessé
Peter van den Bogert

Reviewers
Nick Buik

Prepared for:

EBN B.V.
Daalsesingel 1
3511 SV
Utrecht
The Netherlands

TNO-AGE
Princetonlaan 6
3584 CB
Utrecht
The Netherlands

Prepared by:

PanTerra Geoconsultants B.V.
Weversbaan 1-3
2352 BZ Leiderdorp
The Netherlands
T +31 (0)71 581 35 05
info@panterra.nl

IF Technology B.V.
Velperweg 37
6824 BE Arnhem
The Netherlands
T +31 (0)26 35 35 555
info@iftechnology.nl

Table of Contents

Samenvatting

De nieuwe Seismic Hazard Screening (SHS) methode zal bestaan uit een aantal kernelementen. Dit rapport beschrijft het voorgestelde ontwikkelingsproces, de methode en de resultaten voor één van deze kernelementen: het potentieel voor breukreactivatie. Uiteindelijk wordt dit kernelement gecombineerd met andere kernelementen en door EBN en TNO-AGE samengevoegd tot één nieuwe SHS-methode. In dit samenvoegingsproces kunnen wijzigingen worden aangebracht in de methoden, drempelwaarden en/of resultaten ten opzichte van de afzonderlijke kernelement rapporten. De methoden, waarden en resultaten die in het huidige rapport worden beschreven, moeten daarom als voorlopig worden beschouwd.

Door druk- en temperatuursveranderingen in het reservoir veranderen de spanningen in de ondergrond. De effectieve spanningsveranderingen, genormaliseerd naar druk- en temperatuursveranderingen, kunnen uitgedrukt worden als een functie van dip van een breuk, grootte van de afgekoelde en/of op druk gebrachte regio in het reservoir, en de genormaliseerde juxtapositie van de breuk. In deze studie zijn type curves gecompileerd voor breukreactivatie onder de operationele condities. De type curves zijn geïntegreerd in de screening tool en worden gebruikt om projecten met laag en verhoogd potentieel voor breukreactivatie te onderscheiden.

Drie voorbeelden gebaseerd op huidige geothermische projecten zijn gebruikt om de screening tool te testen. De drie voorbeelden zijn gespreid gekozen over Nederland, en hebben allen een project-specifieke seismische risico-analyse uitgevoerd. In twee van de drie gevallen kwam uit de screening tool een verhoogd potentieel op breukreactivatie. De project-specifieke analyse had echter aangetoond dat het potentieel laag was. Het verschil kon herleid worden tot het feit dat in het screening tool een conservatieve aanname zit voor het in-situ spanningsregime, gebaseerd op West Nederland. Te overwegen valt om het screening tool aan te passen met meer specifieke in-situspanningsregimes per platform of basin. Verder wordt voorgesteld om onzekerheden en stochastische analyse mee te nemen. Dit kan onderdeel zijn van de toekomstige locatie-specifieke evaluatie.

Depth (m)	2000			
Reservoir thickness (m)	100			
Offset fault (m) (positive for "normal" fault, negative for "reverse" fault)	25			
(Reservoir T minus injection T) (°C)	40			
(Injector FBHP - Reservoir pressure) (bar)	10			
Distance injector - fault (m)	500			
Closest distance cold front - fault (m)	0			
Result of screening calculations				
There is	**LOW**	risk of fault reactivation		
SCU (conservative upper limit)	**0.972**			
Temperature contribution	99%			
Pressure contribution	1%			

Figure 1-1 Inputscherm van de screening tool

1 Introduction

The Ministry of Economic Affairs and Climate Policy has requested EBN and TNO to develop a new method to assess the seismic risk for onshore geothermal projects of the Netherlands. The previous guideline by IF/Q-Con (2016) “Defining the Framework for Seismic Hazard Assessment in Geothermal Projects V0.1” (Q-Con & IF Technology, 2016) was developed in 2016 and should be updated to the current state of the geothermal industry.

The new Seismic Hazard Screening (SHS) method will consist of a number of key-elements. This report describes the suggested development process, method and results for one of these key elements: the fault reactivation potential. Eventually, this key-element will be combined with other key-elements and merged into a single, new SHS method by EBN and TNO-AGE. In this merging process, changes may be made to the methods, values and results as described in the individual key-element reports. The methods, values and results described in the current report should therefore be regarded as preliminary.

In the development of the proposal for the new SHS method, it was concluded that indicative calculations should not be part of the to-be-developed Seismic Hazard Screening (SHS), but can be used as insight into the relative importance of the different factors, especially operating conditions ΔT and ΔP, and under which conditions a geothermal project would still pose a “low” seismic hazard. The work is a generalization to arbitrary reservoirs of a published (analytical) SHA methodology (van den Hoek & Poessé, 2021) that was recently applied to several geothermal field cases in The Netherlands.

Reservoir depletion, pressurization, and/or cooling will result in stress changes. These stress changes will exhibit local concentrations along juxtaposed faults, see Figure 1-1 below for an example (cooling). This is not unlike the case made for depleted gas fields (van den Bogert & van Eijs, 2020). In this figure σ_{nt} and σ_{nn} are the induced changes in effective shear and normal stress along the fault, respectively.

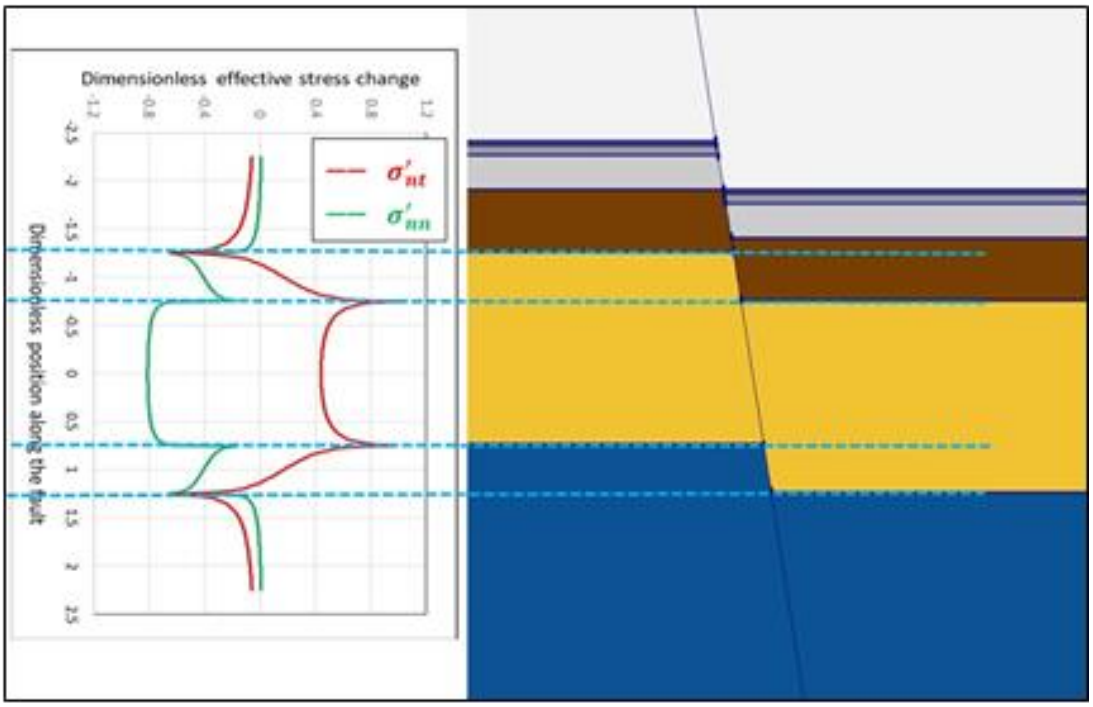

Figure 1-1 Dimensionless effective stress change as a function of cooling along a fault with offset. Green line: normal effective stress, red line: shear stress.

The effective stress changes (normalized to depletion or cooling) can be expressed as a function of fault dip, size of the cooled and / or pressurised zone around injector, and normalized fault juxtaposition.

Within a conservative approach, we apply a "worst-case" fault dip, which for a friction angle of 30° is equal to 0.6 for all faults. This leaves us to study the impact of size of the cooled and / or pressurised zone around injector and normalized fault juxtaposition on effective stress change along the fault. The size of the cooled and/or pressurized zone around a fault *does* have an important impact on stress change as illustrated in figure 1-2. This can be explained via arching by adjacent non-cooled zones.

The above workflow can determine a dimension-less proxy for seismic hazard for given operational conditions ΔT and ΔP. The method is cross-checked with existing tools ("benchmarked").

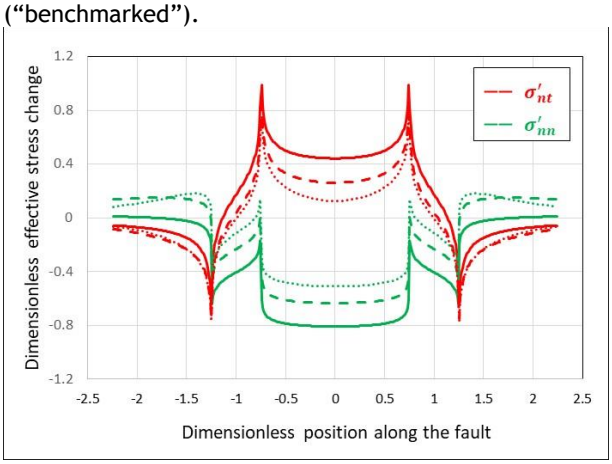

Figure 12 Dimensionless effective stress change as a function of for the example if figure 1-1, where solid, dashed and dotted curves correspond to large, medium and small size of the cooled zone, respectively

This report presents the methodology and modelling exercise to arrive at a tool which can distinguish between “low” and “elevated” fault reactivation risk for given operating conditions. A workflow for using the tool is included and the use and applicability is shown for two known geothermal cases for the Netherlands.

At a later stage, this method could be used as a basis for Monte Carlo calculations to address uncertainties, which has been applied before in geothermal field cases in the Netherlands. The method can be improved upon and combined with learnings from studies into fault reactivation currently being run under the WarmingUp programme (https://www.warmingup.info/) and the KEM programme, e.g. KEM15 (https://kemprogramma.nl/blog/view/5a3ab959-6f72-4e34-9ba7-9af80a7d8be0/kem-15-seismic-risk-due-to-cooling-effects-in-geothermal-systems-started).

2 Theory & Methodology

2.1 GENERAL APPROACH

The effective stress changes (normalised to cooling or depletion) are defined as follows:

$$\Delta\sigma'_{ijD} = \frac{\Delta\sigma'_{ij}}{(\Delta T \text{ or } \Delta p)} \tag{0}$$

They can be expressed as a function of fault dip, dimensionless size of the cooled and / or pressurised zone around injector, and normalised fault juxtaposition (normalised with respect to reservoir layer thickness). Within a conservative approach, we apply a "worst case" fault dip of around 60° for all faults. This leaves us to study the impact of dimensionless size of the cooled and / or pressurised zone and normalised fault juxtaposition on effective stress change along the fault.

We have developed dimensionless 'type curves' of stress changes (normalised to ΔT or Δp, see equation (0)) as a function of size of the cooled and / or pressurised zone and fault juxtaposition, using the methodology of van den Hoek and Poessé (2021). As a next step, this has been coupled to a typical (West-) Netherlands (initial) in-situ stress regime, i.e. vertical and horizontal stresses as a function of depth. The combination of initial in-situ stresses, dimensionless stress changes (including stress concentration and arching effects) and operational / reservoir parameters immediately yield a profile of Shear Capacity Utilisation (SCU) along faults for each project. From such a profile, qualitative criteria have been derived for low versus elevated risk of fault reactivation. Such a risk could be further elaborated by means of a Monte Carlo exercise in which the main uncertainties are addressed (this was outside the scope of this project).

The SCU is defined as follows:

$$SCU = \frac{\tau}{\tau_{max}} = \frac{\sigma'_{nt}}{C + \sigma'_{nn}\tan(\varphi)} \tag{1}$$

where σ'_{nt} and σ'_{nn} are the shear and normal (effective) stresses along the fault respectively, C is the fault cohesion and φ the (static) friction angle. The criterion to avoid fault reactivation is given by

$$SCU < 1 \tag{2}$$

For a fault with a dip angle ϑ and cooling ΔT (= $T_{\text{reservoir}} - T_{\text{injection}}$, in °C) the expression of the SCU (1) can be elaborated as follows:

$$SCU = \frac{\sigma'_{nt0} - A_T \Delta T . \Delta\sigma'_{ntD}}{C + (\sigma'_{nn0} + A_T \Delta T . \Delta\sigma'_{nnD}).tan(\varphi)}$$
$$\sigma'_{nt0} = \frac{1}{2}(1 - k')\sigma'_v sin(2\vartheta)$$
$$\sigma'_{nn0} = \frac{1}{2}(1 + k')\sigma'_v + \frac{1}{2}(1 - k')\sigma'_v cos(2\vartheta) \tag{3}$$

where $\Delta\sigma'_{ntD}$ and $\Delta\sigma'_{nnD}$ are the dimensionless changes in shear stress and normal effective stress along the fault, respectively, σ'_{nt0} and σ'_{nn0} are the shear and normal (effective) *initial* stresses (in Pa) along the fault, respectively, and A_T is the thermo-elastic constant in Pa/°C. The constant k'

in (3) is given by the ratio between *initial* minimum horizontal effective and vertical effective stresses ('initial' = before cooling and / or pressure change):

$$k' = \frac{\sigma'_h}{\sigma'_v} \tag{4}$$

Equations (1)-(4) can be combined to yield the following expression:

$$\frac{|A_T \Delta T|}{\sigma'_v} \cdot \left(\Delta\sigma'_{ntD} + tan(\varphi) \cdot \Delta\sigma'_{nnD}\right) < \boldsymbol{f}(\, C, k', \vartheta, \tan(\varphi)\,) \tag{5}$$

where the function f is given by

$$\boldsymbol{f}(\, C, k', \vartheta, \tan(\varphi)\,) = \frac{C}{\sigma'_v} + \left[\frac{1}{2}(1+k') + \frac{1}{2}(1-k')cos(2\vartheta)\right] tan(\varphi) - \frac{1}{2}(1-k')sin(2\vartheta) \tag{6}$$

For a given (fixed) value of the friction angle φ, equations (5) and (6) enable separation of the generic dimensionless type curves for $\Delta\sigma'_{ntD}$ and $\Delta\sigma'_{nnD}$ from reservoir-specific parameters, such as cooling, depth ($\rightarrow \sigma'_v$) and strength parameters.

Equation (5) shows that an increase in SCU is directly related to an increase in the parameter $\Delta\sigma'_{ntD} + tan(\varphi) \cdot \Delta\sigma'_{nnD}$ which can be captured in generic type curves. The function f only depends on depth, dip angle and strength parameters and is therefore fully given by global (initial) reservoir parameters, i.e. not on cooling, pressure, position of thermal front etc. Cooling, pressure, position of the thermal front etc. are entirely captured by the type curves.

The function f can be looked upon as an "upper limit" for thermal stress changes. For zero fault cohesion C, this function is illustrated in Figure 2-1. As can be seen, the lowest (most conservative) value is obtained for ϑ = 60°, in line with the fact that for a friction angle of 30° the (fault) plane of failure is equal to 60°. This is the value for ϑ that will be further used throughout this report. It can also be seen from figure 2-2 that f strongly decreases with decreasing k' below 1. This is because k'=1 represents an isotropic stress state, and lower values imply larger differential stresses and therefore easier failure. We will come back to this later in the report.

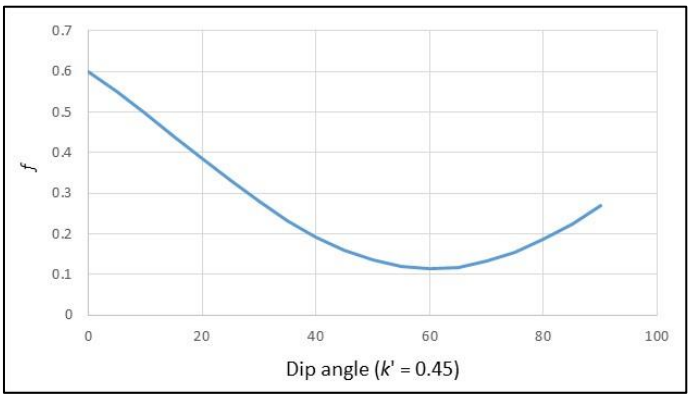

Figure 2-1 Function f versus dip angle ϑ for k' = 0.45

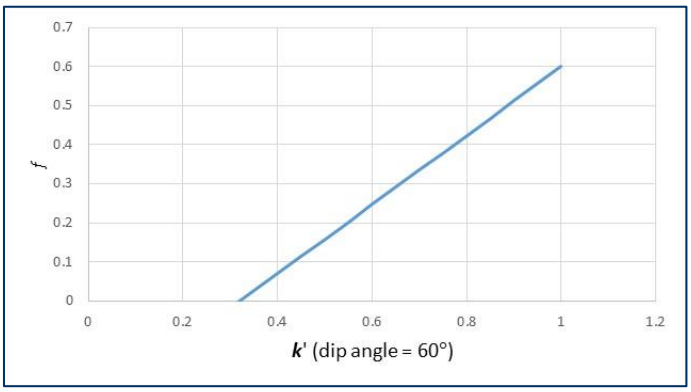

Figure 2-2 Function f versus k' for dip angle $\vartheta = 60°$

2.2 TYPE CURVES FOR TEMPERATURE (COOLING)

Type curves for $\Delta\sigma'_{ntD} + tan(\varphi).\Delta\sigma'_{nnD}$ have been computed for a cold front approaching and crossing a *permeable* fault for a fixed value of tan(φ) = 0.6. The type curves have been computed using the methodology of van den Hoek and Poessé (2021), in which effects of both vertical and horizontal thermal diffusion on the temperature front have been taken into account.

2.2.1 Cold front approaching the fault

Figure 2-3 and Figure 2-4 show the type curves for $\Delta\sigma'_{ntD} + tan(\varphi).\Delta\sigma'_{nnD}$ as a function of dimensionless distance of the cold front from the fault, where the dimensionless distance is defined by:

$$\text{Dimensionless distance} = \frac{\text{Distance}}{\text{Reservoir thickness}} \tag{7}$$

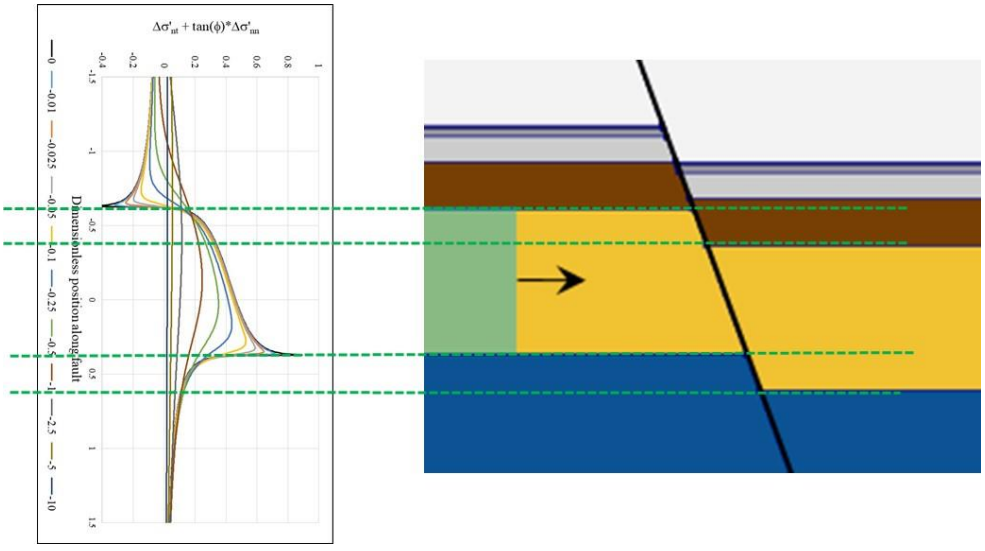

Figure 2-3 Illustration of type curves for $\Delta\sigma'_{ntD} + tan(\varphi).\Delta\sigma'_{nnD}$ for a thermal front approaching the fault

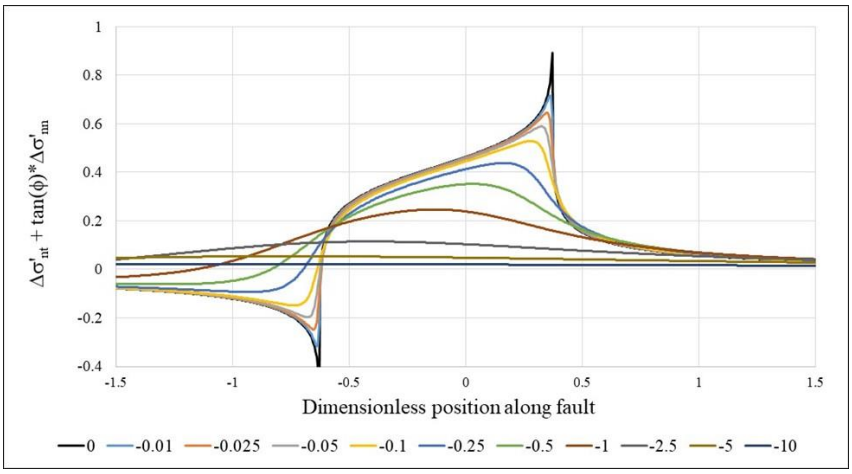

Figure 2-4 Type curves for $\Delta\sigma'_{ntD} + tan(\varphi).\Delta\sigma'_{nnD}$ for a thermal front approaching the fault as a function of dimensionless distance from the fault (minus signs to indicate approach from the left). Position 0 along the fault is defined as the centre between top of foot wall and bottom of hanging wall.

As can be seen from this figure, the maximum value of $\Delta\sigma'_{ntD} + tan(\varphi).\Delta\sigma'_{nnD}$ strongly decreases with increasing distance for distances smaller than the layer thickness. This is also shown in Figure 2-5 and Figure 2-6.

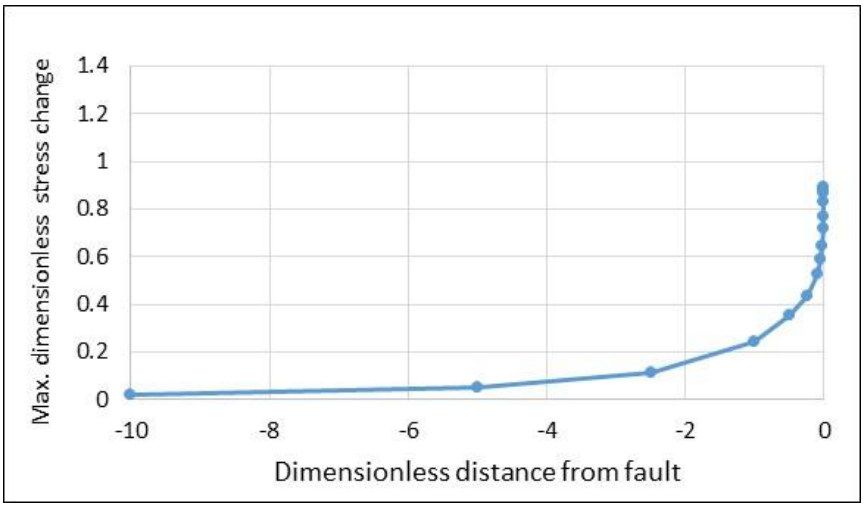

Figure 2-5 Maximum value of $\Delta\sigma'_{ntD} + tan(\varphi).\Delta\sigma'_{nnD}$ for a thermal front approaching the fault as a function of dimensionless distance from the fault (minus signs to indicate approach from the left).

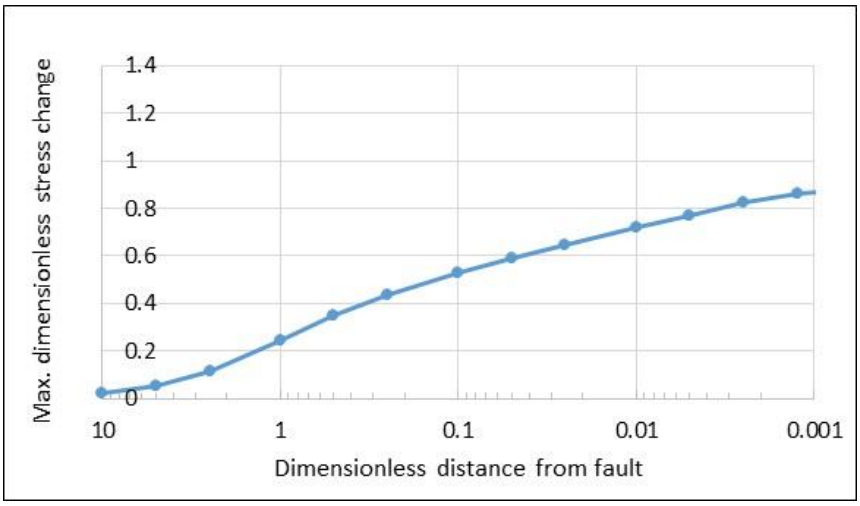

Figure 2-6 Maximum value of $\Delta\sigma'_{ntD} + tan(\varphi).\Delta\sigma'_{nnD}$ for a thermal front approaching the fault as a function of dimensionless distance from the fault (logarithmic scale).

2.2.2 Cold front crossing a permeable fault

Details of a thermal front crossing a tilted permeable fault with offset are complicated and require a full reservoir simulation. Looking at figure 2-3, the thermal front shape (following behind the fluid flow) is expected to become tilted with its bottom more advanced because of the higher horizontal flow rate near the bottom. After crossing the fault, the bottom of the front is expected to 'drop' to the bottom of the hanging wall layer under the influence of gravity (depending on the ratio of vertical permeability over horizontal permeability and density difference between cold and hot water).

The main impact of cold front position upon possible stress concentrations along the fault will be at the sharp angles at the bottom of the top (foot wall) layer and the top of the bottom (hanging wall) layer. In order to keep calculations tractable and remain conservative, it is assumed that the thermal front crosses the fault with a tilted shape that is parallel to the fault. In such a way, the cold front hits the entire (exposed part of the) fault *at once* at a moment in time that no vertical smearing of temperature by thermal diffusion has taken place yet, and therefore the impact of stress concentrations is maximum (van den Hoek and Poessé, 2021). Hitting the entire (exposed part of the) fault at once will have a stronger impact than gradually hitting parts of the fault over time. As a quality check, it was also found that the difference in computed stress concentrations between vertical and tilted thermal fronts is negligible for thermal front penetrations (into the layer on the other side of the fault) equal to the layer thickness or more.

Figure 2-7 to 2-12 illustrate the type curves of $\Delta\sigma'_{ntD} + tan(\varphi).\Delta\sigma'_{nnD}$ as a function of dimensionless time t_D since crossing a permeable fault with dimensionless offset 0.25. Here, the dimensionless time t_D is defined as:

$$t_D = \frac{\eta t}{h^2} \tag{8}$$

where η is the thermal diffusivity, t is the time since crossing the fault, and h is the reservoir thickness. The dimensionless offset is defined by

$$\text{Dimensionless offset} = \frac{\text{Offset}}{\text{Reservoir thickness}} \tag{9}$$

The offset is defined such that a positive offset corresponds to a “normal” fault geometry (hanging wall below the foot wall, see Figure 2-7), whereas a negative offset corresponds to “reverse” fault geometry (hanging wall above the foot wall).

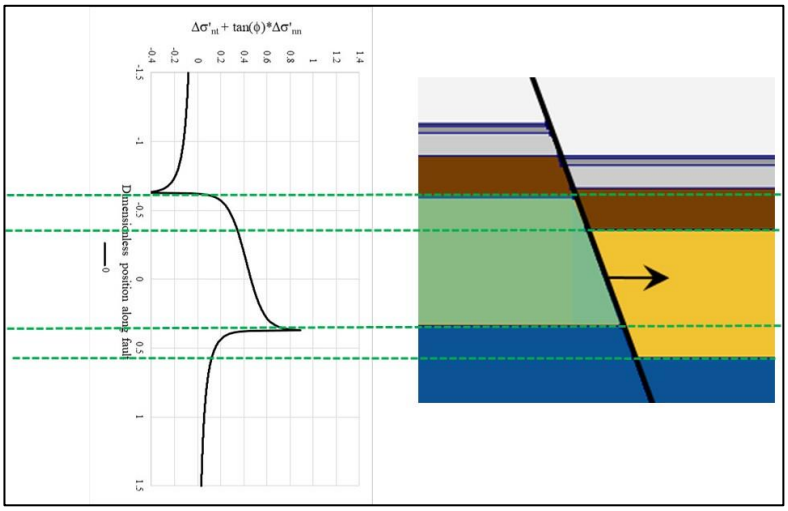

Figure 2-7 Type curve of $\Delta\sigma'_{ntD} + tan(\varphi).\Delta\sigma'_{nnD}$ for the moment that the cold front touches the fault (t_D = 0). This corresponds to the black curve (distance = 0) in Figure 2-4. Position 0 is defined as the centre between top of foot wall and bottom of hanging wall (same as in Fig. 2.4).

Finally, all results shown in this paragraph have been computed for a (conservative) dimensionless injection rate Q_D = 500, where Q_D is defined by

$$Q_D = \frac{Q}{2\pi h\eta}\frac{C_w}{C} \tag{10}$$

with Q the injection rate, C_w and C the specific heats of water and fluid-filled formation, respectively, and h and η as defined above. For “typical” values of C_w (4MJ/m3K), C (2.5 MJ/m3K) and η (10^{-6} m2/s) (Koning, 1988, van den Hoek and Poessé, 2021) a Q_D of 500 corresponds to a Q of 350 m^3/hr for h = 50 m and 1400 m^3/hr for h = 200 m. These are very high rates for a geothermal well, and therefore a Q_D of 500 can be considered as high (i.e. conservative).

Under the assumption that the thermal front crosses the fault with a tilted shape that is parallel to the fault, the cold front just “touches” the fault at t_D = 0 (Figure 2-7). The reservoir section to the left of the fault has been entirely cooled, whereas the reservoir section to the right is still “hot” (uncooled). Moreover, at this moment in time thermal diffusion along the fault from cap- and baserock is still very small. Therefore, the type curve for $\Delta\sigma'_{ntD} + tan(\varphi).\Delta\sigma'_{nnD}$ in this case is characteristic for the stress concentrations on the tilted edge of one layer, and this is indeed what is seen in Figure 2-7.

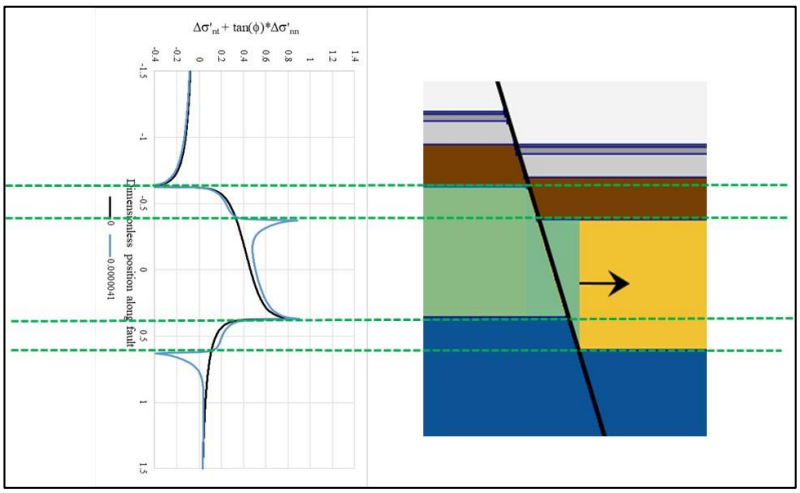

Figure 2-8 Type curve of $\Delta\sigma'_{ntD} + tan(\varphi).\Delta\sigma'_{nnD}$ 'shortly' after the moment that the cold front touches the fault (t_D = 4.10^{-6}). For a reservoir of 200 m thick, this corresponds to 1.5 days. Type curve for t_D = 0 (black line) is also shown in this figure.

Shortly after the cold front has crossed the fault, a small area to the right off the fault is cooled, resulting in a second stress concentration peak above the first one, see Figure 2-8. With increasing time after crossing the fault, the size of the cooled zone to the right of the fault increases as well, and with that the stress concentrations in $\Delta\sigma'_{ntD} + tan(\varphi).\Delta\sigma'_{nnD}$ increase (Figure 2-9 to Figure 2-12). In addition, thermal diffusion into cap- and baserock results in a widening of the stress concentration "mountain" as is visible.

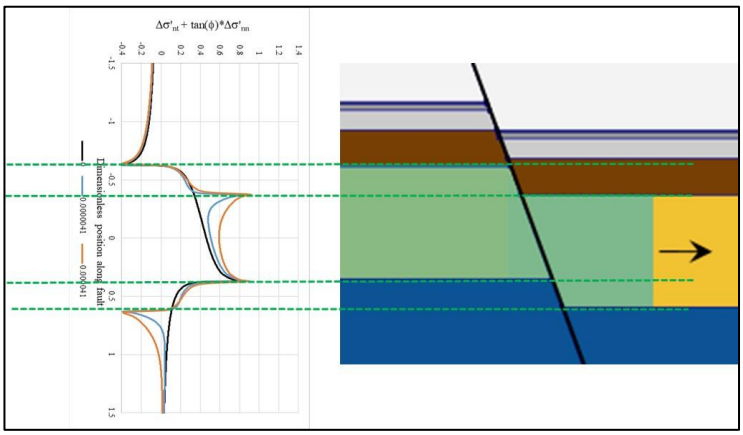

Figure 2-9 Type curve of $\Delta\sigma'_{ntD} + tan(\varphi).\Delta\sigma'_{nnD}$ some time after the moment that the cold front touches the fault (t_D = 4.10^{-5}). For a reservoir of 200 m thick, this corresponds to 15 days. Type curves for t_D = 0 (black line) and t_D= 4.10^{-6} (blue line) are also shown in this figure.

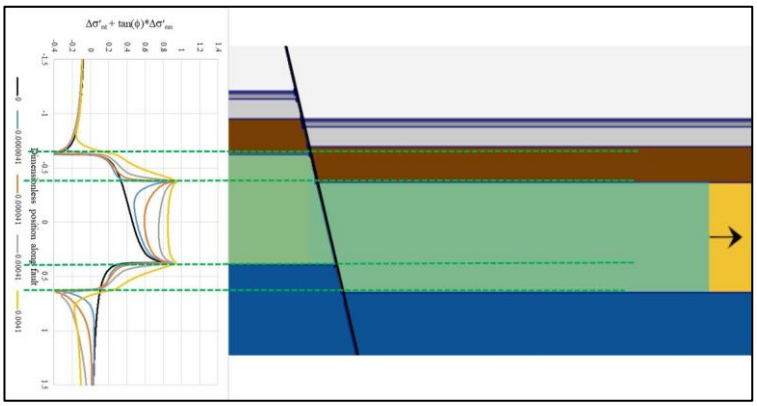

Figure 2-10 Type curve of $\Delta\sigma'_{ntD} + tan(\varphi).\Delta\sigma'_{nnD}$ some time after the moment that the cold front touches the fault (t_D = 0.004). For a reservoir of 200 m thick, this corresponds to 4 years. Type curves for t_D = 0 (black line), t_D= 4.10^{-6} (blue line), t_D= 4.10^{-5} (orange line), and t_D= 4.10^{-4} (grey line) are also shown in this figure.

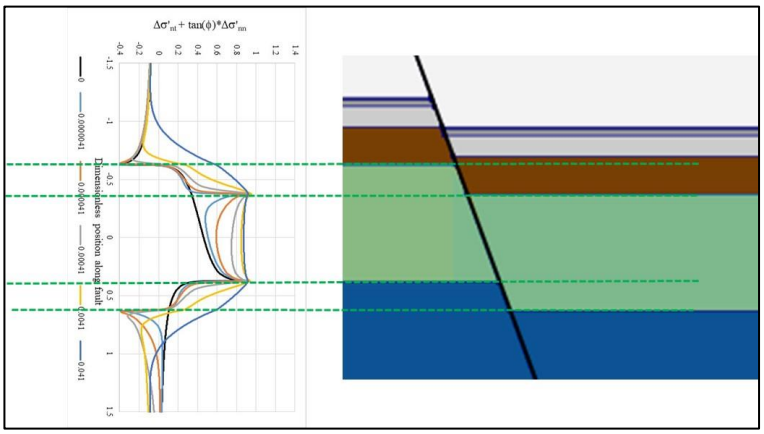

Figure 2-11 Type curve of $\Delta\sigma'_{ntD} + tan(\varphi).\Delta\sigma'_{nnD}$ a long time after the moment that the cold front touches the fault (t_D = 0.04). For a reservoir of 200 m thick, this corresponds to 40 years. Type curves for t_D = 0 (black line), t_D= 4.10^{-6} (blue line), t_D= 4.10^{-5} (orange line), t_D= 4.10^{-4} (grey line) and t_D = 0.04 (yellow line) are also shown in this figure.

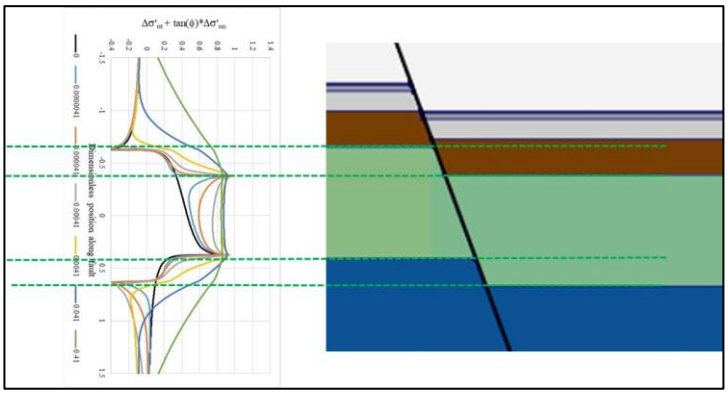

Figure 2-12 Type curve of $\Delta\sigma'_{ntD} + tan(\varphi).\Delta\sigma'_{nnD}$ a very long time after the moment that the cold front touches the fault (t_D = 0.4). For a reservoir of 200 m thick, this corresponds to 400 years, but for a 50 m thick reservoir, this corresponds to (only) 25 years. Type curves for t_D = 0 (black line), t_D= 4.10^{-6} (blue line), t_D= 4.10^{-5} (orange line), t_D= 4.10^{-4} (grey line), t_D = 0.04 (yellow line) and t_D = 0.4 (dark blue line) are also shown in this figure.

In summary, when a cold front crosses a fault, the resulting stress concentrations along the fault will be initially characterized by sharp peaks which over time broaden as a result of further flooding of the reservoir on the other side of the fault and of thermal diffusion within the cap- and baserock.

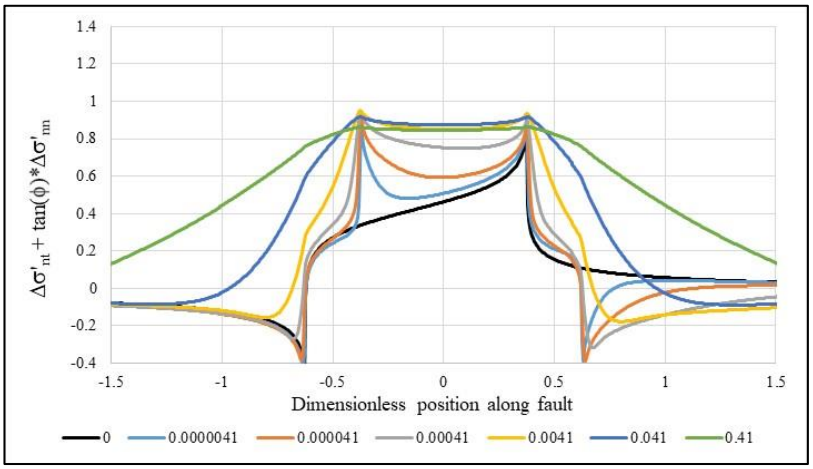

Figure 2-13 Type curves of $\Delta\sigma'_{ntD} + tan(\varphi).\Delta\sigma'_{nnD}$ for a range of dimensionless times t_D after crossing the fault, and for dimensionless offset 0.25.

For a conservative approach, the highest value of SCU is taken along the fault and as a function of time after "touching" the fault by the cold water front. As can be seen from Figure 2-13, this is around t_D = 0.0041 with a corresponding highest value of $\Delta\sigma'_{ntD} + tan(\varphi).\Delta\sigma'_{nnD}$ = 0.95.

Appendix A shows a complete overview of the type curves $\Delta\sigma'_{ntD} + tan(\varphi).\Delta\sigma'_{nnD}$ for all dimensionless offsets. Below, a selection of those is discussed for further physical understanding.

Figure 2-14 shows the same results as Figure 2-13, but now for dimensionless offset 0.9. As can be seen, the highest values of $\Delta\sigma'_{ntD} + tan(\varphi).\Delta\sigma'_{nnD}$ (at t_D = 0.00041 – 0.0041) are significantly higher than for offset 0.25. The reason is that the stress changes resulting from cooling on both sides of the fault are concentrated in a much smaller (fault-overlapping) area. Also, the stress concentrations remain high long-term with increasing thermal diffusion into cap- and baserock because the cooled areas below the foot wall (baserock) and above the hanging wall (caprock) contribute to the stress concentrations. The highest stress concentrations as a function of offset are reached for dimensionless offset = 1 (Figure 2-15), and this drops rapidly for offsets above 1 (Figure 2-16).

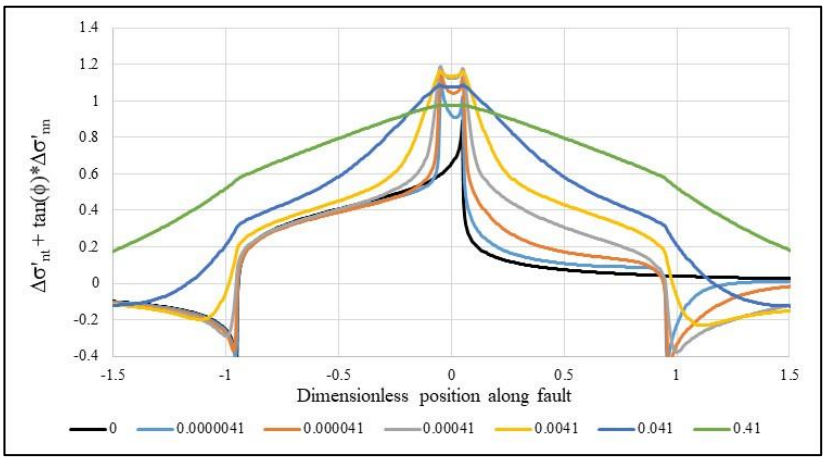

Figure 2-14 Type curves of $\Delta\sigma'_{ntD} + tan(\varphi).\Delta\sigma'_{nnD}$ for a range of dimensionless times t_D after crossing the fault, and for dimensionless offset 0.9.

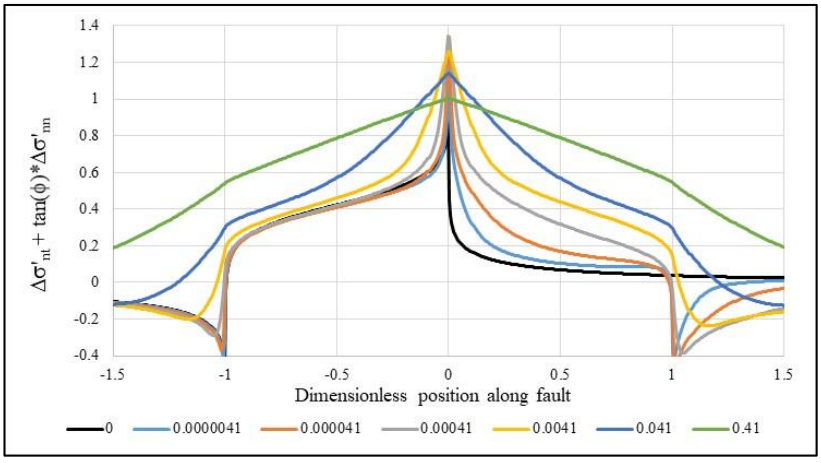

Figure 2-15 Type curves of $\Delta\sigma'_{ntD} + tan(\varphi).\Delta\sigma'_{nnD}$ for a range of dimensionless times t_D after crossing the fault, and for dimensionless offset 1.0.

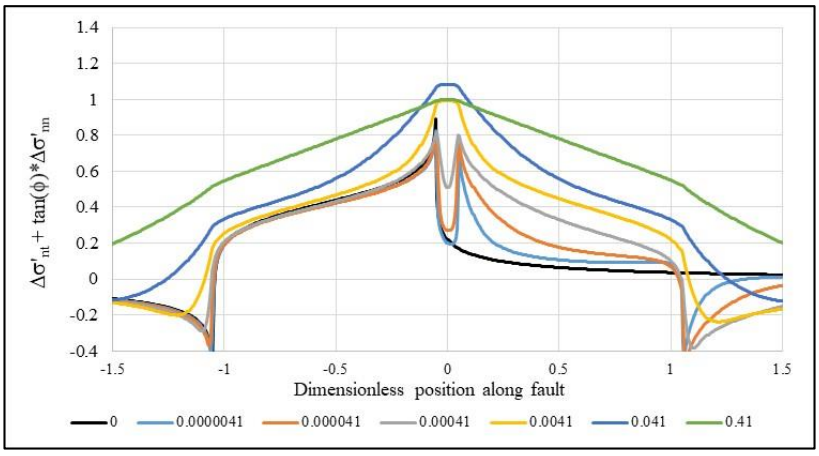

Figure 2-16 Type curves of $\Delta\sigma'_{ntD} + tan(\varphi).\Delta\sigma'_{nnD}$ for a range of dimensionless times t_D after crossing the fault, and for dimensionless offset 1.1.

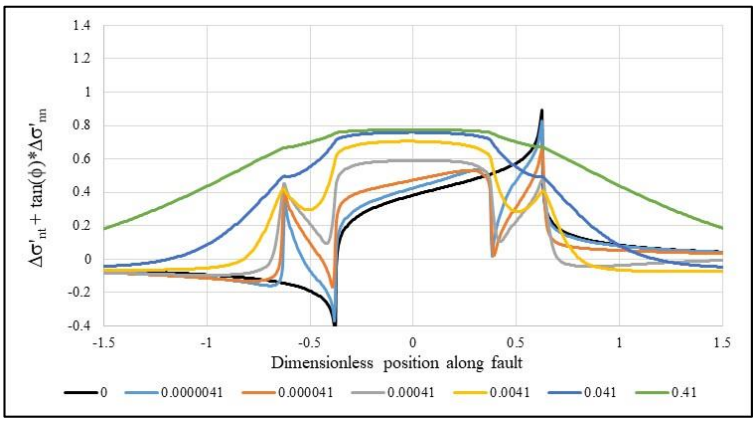

Figure 2-17 Type curves of $\Delta\sigma'_{ntD} + tan(\varphi).\Delta\sigma'_{nnD}$ for a range of dimensionless times t_D after crossing the fault, and for dimensionless offset –0.25.

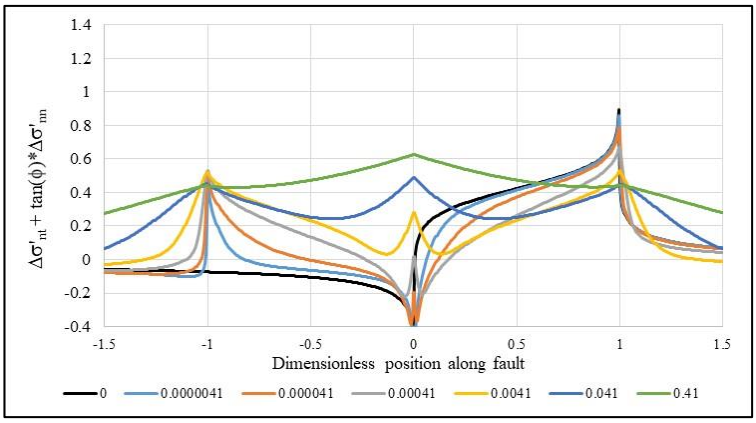

Figure 2-18 Type curves of $\Delta\sigma'_{ntD} + tan(\varphi).\Delta\sigma'_{nnD}$ for a range of dimensionless times t_D after crossing the fault, and for dimensionless offset –1.0.

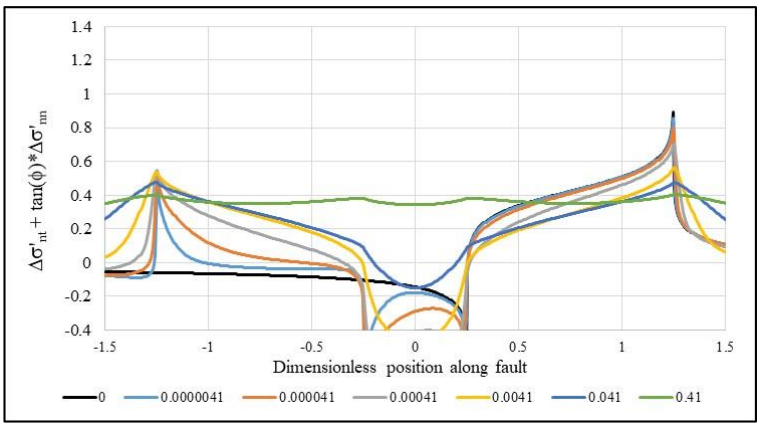

Figure 2-19 Type curves of $\Delta\sigma'_{ntD} + tan(\varphi).\Delta\sigma'_{nnD}$ for a range of dimensionless times t_D after crossing the fault, and for dimensionless offset –1.5.

Figure 2-17 to Figure 2-19 display the type curves of $\Delta\sigma'_{ntD} + tan(\varphi).\Delta\sigma'_{nnD}$ for negative offsets ("reverse" fault geometry). As can be seen from these figures, the type curves exhibit a fundamentally different behaviour than the type curves for positive offsets ("normal" fault

geometry). In fact, for all cases the highest stress concentration is reached right at the start, i.e. at the moment the cold front "touches" the fault.

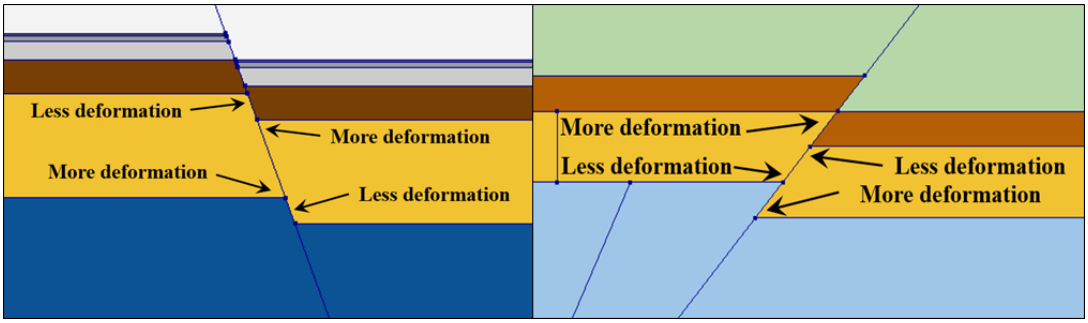

Figure 2-20 Explanation for the fundamentally different characteristics of stress concentrations along the fault between "normal fault" geometries (left) and "reverse fault" geometries (right).

An explanation for the difference between "normal fault" geometry (with two nearby high stress concentrations) and "reverse fault" geometry (with two high stress concentrations that are far apart) is offered in Figure 2-20. This figure indicates areas with more elastic deformation and less elastic deformation following reservoir cooling. Generally speaking, in response to increasing vertical effective stress, a cooling reservoir will tend to exhibit more elastic strain in areas that form a sharp angle with respect to adjacent (non-cooling) formations than in areas that form a dead angle. This makes intuitively sense and is also confirmed by finite element calculations. As a result of these different strain tendencies, the highest shear stresses along the fault are expected to build up adjacent to reservoir areas with the highest deformation tendencies. For the "normal faulting" geometries, this is at the bottom of the top reservoir and the top of the bottom reservoir, whereas for the "reverse faulting" geometries, this is at the top of the top reservoir and the bottom of the bottom reservoir.

Finally, from all the type curves of $\Delta\sigma'_{ntD} + tan(\varphi).\Delta\sigma'_{nnD}$ as a function of position along the fault and of dimensionless time t_D, we take the most conservative value for each fault offset. For example, for a dimensionless offset of 0.25, we arrived at a value of $\Delta\sigma'_{ntD} + tan(\varphi).\Delta\sigma'_{nnD}$ = 0.95 corresponding to the maximum value at time t_D = 0.0041 (see discussion below Figure 2-13). In a similar way, "conservative maximum" values can be obtained for the other offsets.

The result of this exercise is shown in Figure 2-21. This figure clearly displays the general features that were discussed above. For example, the highest value is seen for offset +1, whilst for negative offset, the $\Delta\sigma'_{ntD} + tan(\varphi).\Delta\sigma'_{nnD}$is independent of offset, because it reflects the highest stress concentration at t_D = 0.

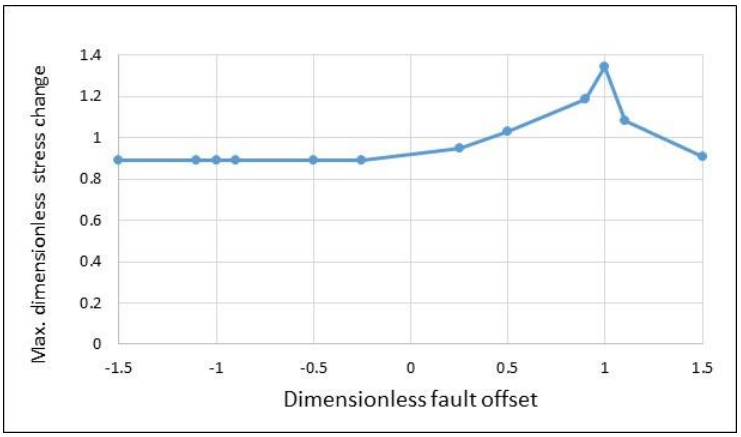

Figure 2-21 Maximum value of $\Delta\sigma'_{ntD} + tan(\varphi).\Delta\sigma'_{nnD}$ for cooling as a function of dimensionless fault offset.

2.3 TYPE CURVES FOR PRESSURE (PRESSURE INCREASE AROUND INJECTOR)

Type curves for $\Delta\sigma'_{ntD} + tan(\varphi).\Delta\sigma'_{nnD}$ have been computed for a a fault at different distances from the injection well. The type curves have been computed using the methodology of van den Hoek and Poessé (2021).

In this case, equation (5) for fault reactivation changes to

$$\frac{|A_p \Delta p|}{\sigma'_v}.\left(\Delta\sigma'_{ntD} + tan(\varphi).\Delta\sigma'_{nnD}\right) < \boldsymbol{f}(\, C, k', \vartheta, \tan(\varphi)\,) \tag{10}$$

where A_p is the poro-elastic constant and Δp the pressure increase in the injector.

The pressure profile around the injector is assumed to have a logarithmic form (R_e = drainage radius),

$$\Delta p(r) \propto ln\left(\frac{R_e}{r}\right) \tag{11}$$

whilst the entire reservoir interval is assumed to be perforated.

For a fault at a certain distance from the injector, eq. (11) can be combined with the methodology of van den Hoek and Poessé (2021) to compute dimensionless stress changes along the fault. In the figures below (and in Appendix B), the computed quantity $\Delta\sigma'_{ntD} + tan(\varphi).\Delta\sigma'_{nnD}$ along the fault is shown for different dimensionless offsets as a function of dimensionless distance, where in this case dimensionless distance is defined as

$$\text{Dimensionless distance} = \frac{\text{Distance injector}-\text{fault}}{\text{Drainage radius}} \tag{12}$$

Figure 2-22 shows the dimensionless stress change $\Delta\sigma'_{ntD} + tan(\varphi).\Delta\sigma'_{nnD}$ along the fault for a number of dimensionless distances d/R_e between injector and fault, and fault offset +0.9. As can be seen from this figure, the dimensionless stress changes are only appreciable for small distances between injector and fault. For example, for a drainage radius R_e = 1000 m, the figure shows that for well-fault distances exceeding about 100 m, the pressure contribution is already fairly small.

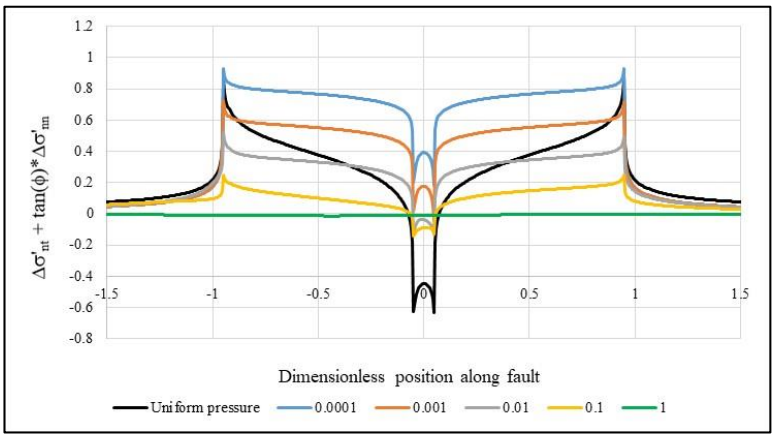

Figure 2-22 Type curves of $\Delta\sigma'_{ntD} + tan(\varphi).\Delta\sigma'_{nnD}$ for a range of dimensionless distances d/R_e between injector and fault, and for dimensionless offset +0.9. For comparison, also the case of uniform pressure increase equal to the injector pressure increase is given (black curve).

Another feature of Figure 2-22 is that qualitatively it is a "mirror image" (in the horizontal axis) of the type curves of $\sigma'_{ntD} + tan(\varphi).\Delta\sigma'_{nnD}$ for the temperature (compare, for example, with Figure 2-14). This can be explained by the fact that cooling tends to *increase* effective stress at the fault, whereas pressure increase tends to *decrease* it. As a result of the geometrical concentration of stress change in the area where the juxtaposed layers overlap, it can be seen that in this case the *decrease* in (compressive) effective stress is most in this area.

Finally, the (black) uniform pressure curve of $\sigma'_{ntD} + tan(\varphi).\Delta\sigma'_{nnD}$ is less uniform along the fault than the other curves. This can be explained by the fact that for uniform pressure (loading), the *total* (not effective) poroelastic stress change will be larger because a significantly larger area (i.e. the entire reservoir) is loaded by the pressure increase. On the other hand, for near-wellbore pressure increase the total poroelastic stress change will be limited, and the main contribution to the effective stress change will be the local pressure increase, see Figure 2-23 for an illustration.

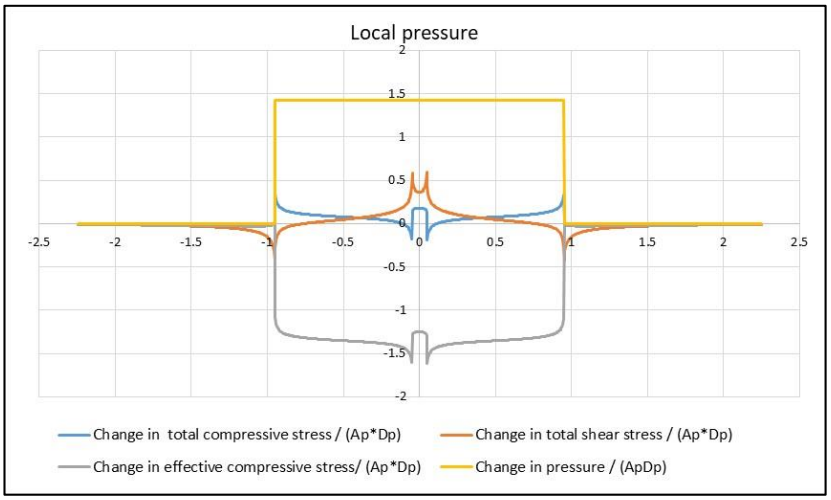

Figure 2-23 Type curves of dimensionless changes in total and effective compressive stress, in shear stress, and in pressure for dimensionless distance d/R_e = 0.0001 between injector and fault, and for dimensionless offset +0.9.

Just like in the case of cooling, from all the type curves of $\Delta\sigma'_{ntD} + tan(\varphi).\Delta\sigma'_{nnD}$ as a function of position along the fault and of dimensionless distance between injector and fault, we take the most conservative value for each fault offset. For example, for a dimensionless offset of 0.9 and

dimensionless distance d/R_e = 0.1, we arrive at a "conservative maximum" value of $\Delta\sigma'_{ntD} + tan(\varphi).\Delta\sigma'_{nnD}$ = 0.19 (see Figure 2-22). In a similar way, "conservative maximum" values can be obtained for the other offsets.

The result of this exercise is shown in Figure 2-24 and Figure 2-25. In this case, the highest value of $\Delta\sigma'_{ntD} + tan(\varphi).\Delta\sigma'_{nnD}$ takes place for dimensionless fault offset −1 (instead of +1) because of the "mirror image" effect as discussed above. This also demonstrates that the pressure contribution to $\Delta\sigma'_{ntD} + tan(\varphi).\Delta\sigma'_{nnD}$ declines rapidly with increasing distance between injector and fault, in line with expectations.

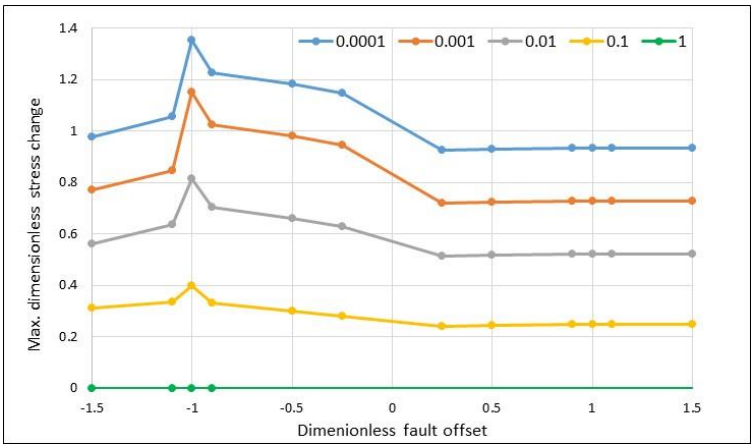

Figure 2-24 Maximum value of $\Delta\sigma'_{ntD} + tan(\varphi).\Delta\sigma'_{nnD}$ for pressure increase as a function of dimensionless fault offset for different values of dimensionless distance d/R_e between injector and fault.

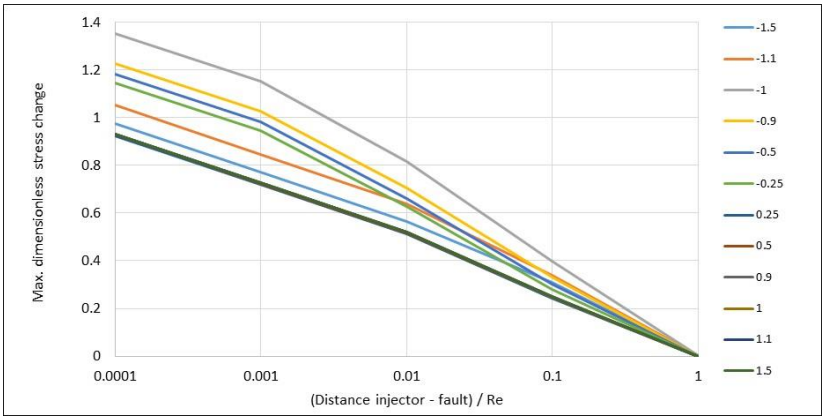

Figure 2-25 Maximum value of $\Delta\sigma'_{ntD} + tan(\varphi).\Delta\sigma'_{nnD}$ for pressure increase as a function of dimensionless distance d/R_e between injector and fault, for different values of fault offset.

2.4 COMBINATION OF TYPE CURVES FOR TEMPERATURE (COOLING) AND PRESSURE (PRESSURE INCREASE AROUND INJECTOR)

For the general case of both cooling and pressure increase, the criterion SCU < 1 corresponds to

$$\frac{|A_T \Delta T|}{\sigma'_v} \cdot \left(\Delta\sigma'_{ntD-T} + \tan(\varphi) \cdot \Delta\sigma'_{nnD-T}\right) + \frac{|A_p \Delta p|}{\sigma'_v} \cdot \left(\Delta\sigma'_{ntD-p} + \tan(\varphi) \cdot \Delta\sigma'_{nnD-p}\right) < \boldsymbol{f}(C,\ k', \vartheta, \tan(\varphi)\ ) \tag{13}$$

Our approach is that we take a combination of conservative values for the temperature and pressure contributions to (13), as based on the type curves of Figure 2-7/2-6 (cooling, in case the cold front does not intersect a fault), Figure 2-21 (cooling, in case the cold front intersects a fault), and Figure 2-24/Figure 2-25 (pressure). Therefore, both the cooling and the pressure terms will be positive, and there will be no "compensation" effect of one by the other.

For example, for a case where the cold front crosses a fault with a dimensionless offset of 0.5 which is located at 0.1*R_e from the injector, 2-5/2-6, Figure 2-21 and Figure 2-24/Figure 2-25 can be read off to arrive at the following equation:

$$\frac{|A_T \Delta T|}{\sigma'_v} * 1.02 + \frac{|A_p \Delta p|}{\sigma'_v} * 0.25 < \boldsymbol{f}(C,\ k', \vartheta, \tan(\varphi)\ ) \tag{14}$$

in which all parameters can be directly derived from depth, regional stress regime, cooling, pressure increase at the injector, and material strength parameters.

3 Description and use of the tool

3.1 DESCRIPTION

The results as presented in chapter 2 and Appendices A and B have been incorporated into a spreadsheet tool that computes its results by interpolating between dimensionless type curves as presented in chapter 2. As explained in 2.1, this is an easy exercise because the type curves contain no information about specific reservoirs other than dimensionless offset, dimensionless distance of the cold front from the fault, and dimensionless distance of the injector well from the fault.

3.2 LIST OF 'CONSERVATIVE' ASSUMPTIONS AND VALUES

1. Fault tilt angle = 60°.
2. Thermal front hits the fault 'at once' → maximum stress concentration effect.
3. High dimensionless injection rate Q_D = 500 → maximum impact of cooling.
4. From the entire profile of $\Delta\sigma'_{ntD} + tan(\varphi).\Delta\sigma'_{nnD}$ along the fault, use the maximum value (applies for both temperature and pressure).
5. From maximum values of $\Delta\sigma'_{ntD} + tan(\varphi).\Delta\sigma'_{nnD}$ as a function of field life, use the maximum value (applies for both temperature and pressure).
6. In adding up the impact of cooling and pressure on stress concentrations along the fault, add up maximum values in order to prevent (partial) 'compensation' of one by the other.
7. Fault is fully permeable → cooling on the 'other side' of the fault also contributes to stress concentrations along the fault.
8. Fault cohesion C = 0.
9. Friction angle φ of fault: tan(φ) = 0.6.
10. k' as defined by equation (4) is for West Netherlands conditions → maximum deviatoric stress.
11. Drainage radius R_e = 1000 m → maximum pressure effect on stress changes along fault
12. (Depth: top of reservoir → lowest σ'_v in equation (13))

3.3 LIST OF OTHER VALUES OF 'FIXED' PARAMETERS

1. Total overburden gradient = 0.22 bar/m
2. Pore pressure gradient = 0.104 bar/m
3. Poro-elastic constant A_p = 0.7
   REMARK: the theoretical formula for A_p is given by $A_p = (1-\beta)\frac{1-2\nu}{1-\nu}$. However, lab tests and also field calibrations have shown that this formula is a 'rough approximation' at best. Therefore, it is proposed to use (a) field-calibrated value(s).
4. Thermo-elastic constant A_T = 1 bar/°C
   REMARK: the theoretical formula for A_T is given by $A_T = \frac{\alpha E}{1-\nu}$. However, lab tests and also field calibrations have shown that this formula is a 'rough approximation' at best. Therefore, it is proposed to use (a) field-calibrated value(s).

3.4 INPUT

Table 3-1 Variable input for the tool

Depth (m)	2000
Reservoir thickness (m)	200
Offset fault (m) (positive for "normal" fault, negative for "reverse" fault)	50
(Reservoir T minus injection T) (°C)	40
(Injector BOP - Reservoir pressure) (bar)	10
Distance injector - fault (m)	500
Closest distance cold front - fault (m)	0

This table has a very limited input, thus allowing no “tweaking” of parameters to obtain a favorable outcome.
The result is computed by evaluating equation (13) in combination with interpolation between the results of Figure 2-7/2-6, Figure 2-21 and Figure 2-24/Figure 2-25. Also, from the interpolated result plus the reservoir-specific parameters, an appropriate value of conservative upper limit of the SCU is computed.

3.5 OUTPUT

Depth (m)	2000			
Reservoir thickness (m)	100			
Offset fault (m) (positive for "normal" fault, negative for "reverse" fault)	25			
(Reservoir T minus injection T) (°C)	40			
(Injector FBHP - Reservoir pressure) (bar)	10			
Distance injector - fault (m)	500			
Closest distance cold front - fault (m)	0			
Result of screening calculations				
There is	**LOW**	risk of fault reactivation		
SCU (conservative upper limit)	**0.972**			
Temperature contribution	99%			
Pressure contribution	1%			

Figure 3-1 Input screen of the tool showing default input

The output appears right below the input. Based on the computed SCU, a “green area” ($0 \leq SCU < 0.995$), and a “red area” ($SCU \geq 0.995$) are defined. The boundary between “green” and “red” has been somewhat arbitrarily chosen at 0.995 and can be changed easily in the future.
In addition, the relative contributions of cooling and pressure increase are indicated. As discussed in chapter 2, the relative contribution from pressure is generally expected to be minor.

3.6 FIXED VALUES

Fixed values within the tool are indicated in the table below. These values can be changed based on the outcome of future discussions between experts.

Table 3-2 Fixed values within the tool

C (bar)	0	Cohesion of fault
tan(ϕ)	0.6	φ = friction angle of fault
Effective overburden gradient (bar/m)	0.116	Overburden gradient minus pore pressure gradient
k'	computed internally	Defined by equation (4). This ratio increases with depth (Verweij *et al.*, 2012)
ϑ(°)	60	Inclination of fault
A_p	0.7	Poro-elastic constant
A_T (bar/°C)	1	Thermo-elastic constant
Drainage radius (m)	1000	Half of distance between injector and producer

As it turns out, results are very sensitive to the ratio k' between effective minimum horizontal stress and effective vertical stress. Generally, this ratio increases with increasing depth. Currently, a trend curve based on data from the West Netherlands basin (Verweij, Simmelink, Underschultz, & Witmans, 2012) has been incorporated. This trend curve is based on the following equation for total minimum horizontal stress.

$$\sigma_h\,(\text{MPa}) = \left[\frac{\text{Depth (m)}}{68.223}\right]^{\left(\frac{1}{0.9675}\right)} \quad (15)$$

Using an overburden gradient of 0.22 bar/m and a pore pressure gradient of 0.104 bar/m, equation (15) immediately yields a value of k' as a function of depth.
If new data would be available that warrants a change in any of the above parameters this can be changed directly in the tool without impacting the results from the type curve study.

3.7 VALIDATION OF THE TOOL

Goodier (1937) developed an analytical solution for the stress change in an arbitrary point in the subsurface as a result of pressure depletion in a rectangular reservoir in a two-dimensional infinite medium. Nowacki (1986) derived a similar analytical solution for a rectangular depleting reservoir in an elastic X f-space (Figure 3-2a). The main difference between these two solutions is the presence of a stress-free surface. For sX low reservoirs, say up to 1000 m depth, the nearby stress-free surface does impact the calculated stress change and Nowacki's solution is preferred. For deeper reservoirs, as in most geothermal projects in the Netherlands, the stress-free surface is sufficiently far away and Goodier's solution is sufficiently accurate.

The stress change in the subsurface of a trapezoid reservoir is required to calculate the stress distribution along a dipping fault plane at the right-hand side of a depleting reservoir ((Figure 3-2b). For vertical faults with a dip angle of 90 degrees, Goodier's (1937) or Nowacki's (1986) solution can be used to calculated the stress change along a vertical line at the right-hand side of the rectangular depleting reservoir. However, the accuracy of the solution deteriorates with

reducing dip angle. For this reason, Lehner (2019, (Figure 3-2b) derived an analytical solution for a trapezoid reservoir in an infinite plane-strain medium (similar to Goodier).

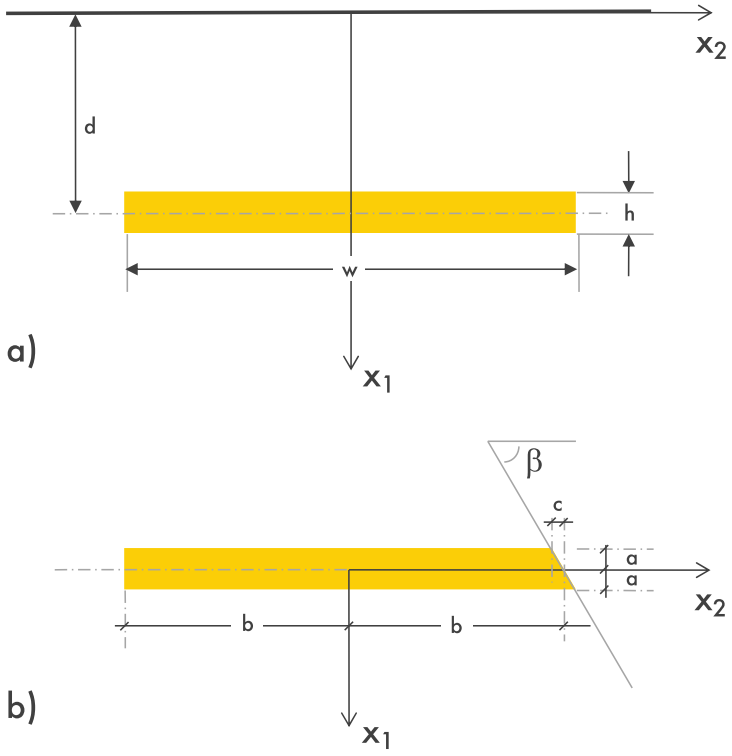

Figure 3-2 a) Nowacki's (1986) rectangular plane-strain reservoir with stress-free surface, and b) Lehner's (2019) trapezoid plane-strain reservoir without stress-free surface (at arbitrary depth).

Van den Bogert (2019) used Lehner's solution to validate Finite-Element results and develop a fast analytical approach to fault rupturing in depleting reservoirs. In this Appendix the analytical solution used in this study is compared to both the analytical solution by Lehner and the finite-element results by van den Bogert (2019).

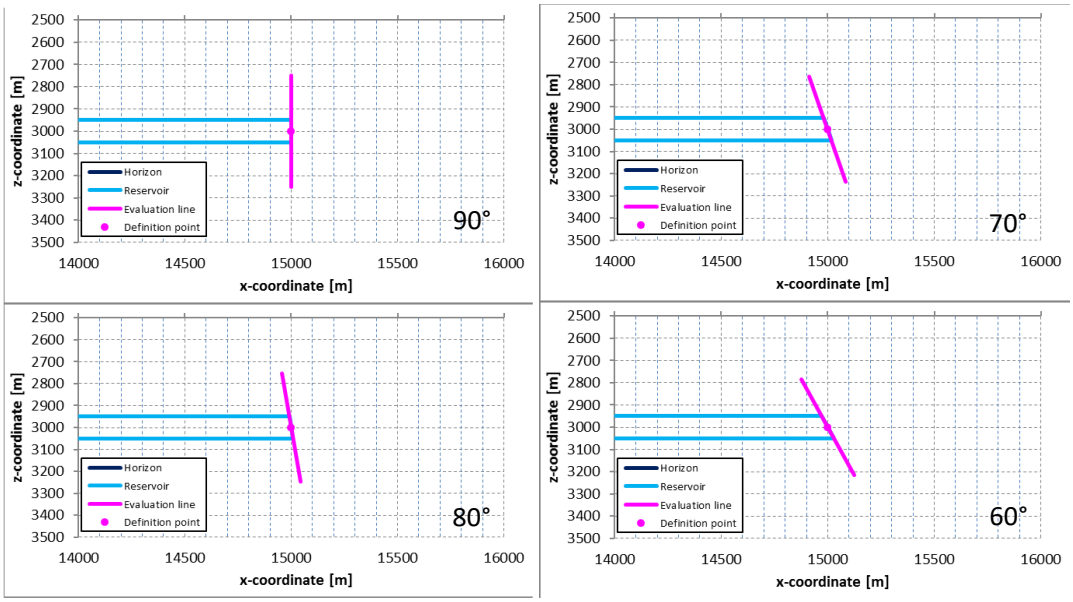

Figure 3-3 Foot wall reservoir bounded by a fault dipping under 90, 80, 70 and 60 degrees respectively (Van den Bogert, 2019).

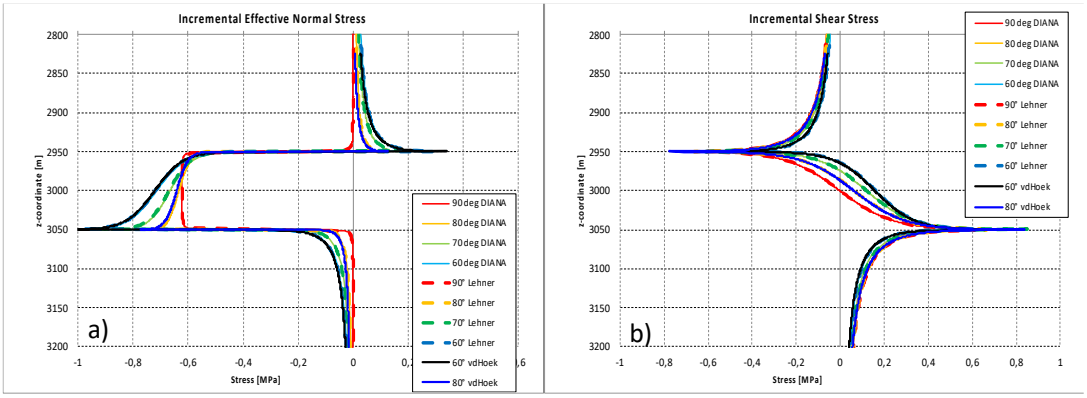

Figure 3-4 a) Incremental effective normal stress, and b) the incremental shear due to 1 MPa reservoir depletion along fault planes dipping under 90, 80, 70 and 60 degrees (Van den Bogert, 2019). The analytical solution used in this study for 60 and 80 degree dip angle is represented by the black and blue solid lines respectively (labelled "60° vdHoek" and "80° vdHoek").

Figure 3-3 shows a foot wall reservoir bounded by a fault (purple line) dipping under 90, 80, 70 and 60 degrees respectively, while Figure 3-4 shows the change in normal effective stress along the fault plane due to a reduction of the reservoir pressure of 1 MPa. It is seen that the analytical solution used in this study corresponds exactly with the Lehner's (2019) analytical solution and the DIANA finite-element results as reported by Van den Bogert (2019).

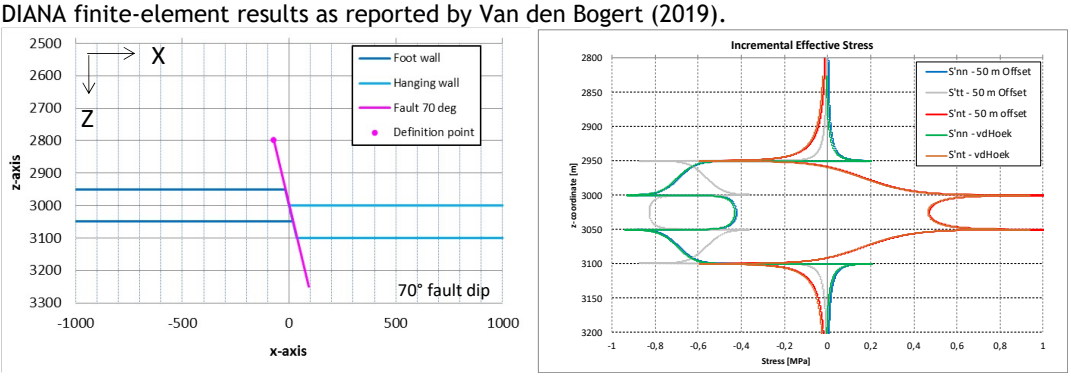

Figure 3-5 a) Fault plane dipping under 70 degrees offsetting an infinite 100 m thick reservoir by 50 m, and b) the change of normal effective stress and shear stress along the fault plane due to a reservoir depletion of 1 MPa (Van den Bogert, 2019).

Figure 3-5 shows the change of effective normal stress and shear stress along a fault dipping under 70 degrees that offsets a horizontally infinite reservoir of 100 m thick by 50 m (normalised reservoir offset 0.5). The results are given for the analytical solutions used in this study and by Lehner (2019), which are identical to the DIANA finite-element results as reported by Van den Bogert (2019). It is concluded that results from the analytical solution used in this study are identical to those obtained by other authors using analytical and finite-element approaches.

4 Field validation

4.1 FIELD EXAMPLES

Three actively operating geothermal projects are used to compare and validate the use of the tool. The cases reflect the majority of the subsurface projects in the Netherlands. The presented cases are a project in Noord-Holland, Centraal Nederland and Zuid-Holland. For each of the projects, a project-specific analysis is available. The results from this analysis are compared with the simplified approach provided by the newly developed screening tool. The tool is currently designed to be more conservative than a location-specific analysis as the field examples show.

The project in Zuid-Holland makes use of the Jurassic Delft/Alblasserdam Sandstone reservoir which is the main target in the West of the Netherlands. It is located in the West-Netherlands Basin which is considered the most conservative setting of the stress regime (see section 3.5). The project in Centraal Nederland on the other hand sources from the Slochteren reservoir, being the main target in the Northern part of the Netherlands. The area is also slightly overpressured and it exhibits larger temperature differences than the project in Zuid-Holland. The project in Noord-Holland also sources the Slochteren reservoir but is in its depth and temperature differential are one of the highest currently in operation.

4.2 PROJECT ZUID-HOLLAND

A project-specific hazard analysis was available. Injector and producer are clearly on different sides of a fault zone. The fault area is expected to cool down and the geomechanical state and fault reactivation potential under operating conditions was assessed. The results of the SHA were positive with an SCU value in the order of 0.7. Assessing the case with the screening tool the resulting SCU is higher due to the conservative nature of the tool. This is mainly caused by the following items:

- The k' for the West-Netherlands Basin is taken more conservatively in the tool. Local FIT and LOT tests can allow for a more deterministic approach in terms of the k' as was used for the location-specific case of X.
- In the project-specific analysis, temperature diffusion is addressed fully in 2D space, resulting in less stress concentration along fault planes, providing again a more deterministic view. The prepared tool does not compensate for horizontal diffusion at offset along a fault plane nor does it contain a depth-dependent thermal gradient. It is likely including these factors may provide a less conservative estimate of the situation. It is likely including these factors may provide a less conservative estimate of the situation. Whether this difference is of significance must be assessed in a more site-specific analysis. The lack of these physics in the tool result in a more conservative estimate of the situation as is the purpose of this SHS key-element.

Depth (m)	1975				
Reservoir thickness (m)	100				
Offset fault (m) (positive for "normal" fault, negative for "reverse" fault)	-25				
(Reservoir T minus injection T) (°C)	28				
(Injector FBHP - Reservoir pressure) (bar)	12				
Distance injector - fault (m)	300				
Closest distance cold front - fault (m)	0				
Result of screening calculations					
There is	**LOW**	risk of fault reactivation			
SCU (conservative upper limit)	**0.843**				
Temperature contribution	95%				
Pressure contribution	5%				

Figure 4-1 The tool applied to the Zuid-Holland case

4.3 PROJECT CENTRAAL NEDERLAND

For this project, the project-specific analysis assumed the stress differentials caused by temperature and pressure change affect the fault directly. The risk was assessed as low, no SCU value was provided. In practice, the fault is not expected to be affected ("Closest distance cold front – fault" > 0), which would only further lower the risk. The result from the screening tool reaches SCU value 1.0 however. This can mostly be attributed to the larger temperature differential and the assumption that the cold front is crossing the fault at 800m distance. Under the conservative conditions the tool determines the risk to be elevated, warranting a location-specific analysis, which would prove the risk is lower than the tool indicates.

Depth (m)	1850				
Reservoir thickness (m)	80				
Offset fault (m) (positive for "normal" fault, negative for "reverse" fault)	80				
(Reservoir T minus injection T) (°C)	42				
(Injector FBHP - Reservoir pressure) (bar)	6				
Distance injector - fault (m)	800				
Closest distance cold front - fault (m)	0				
Result of screening calculations					
There is	**ELEVATED**	risk of fault reactivation			
SCU (conservative upper limit)	**1.000**				
Temperature contribution	100%				
Pressure contribution	0%				

Figure 4-2 The tool applied to the Centraal Nederland case

Other differences between the tool and the project-specific analysis are as follows:

- The value used for k' was taken much more conservatively than known for the Netherlands. The PSNS database (TNO, 2015) suggests a k' in the order of 0.50 for the region, based on local FIT and LOT tests. This is partially caused by the slightly overpressured reservoir (by about 10 bar) but mostly caused by an over-conservative estimate of the stress gradient. It should be noted that overpressure can be corrected for by applying it as excess "Injector FBHP - reservoir pressure" in the tool.
- The analysis previously performed did not include stress concentration along the fault plane due to the offset at a fault. Assuming the offset of '1' at the fault plane the new tool projects a more conservative scenario.

4.4 PROJECT NOORD-HOLLAND

The project-specific analysis concluded a low risk for fault reactivation with an SCU value of around 0.75. For this, a small fault was analysed close to the injector. The large temperature differential causes the results screening tool to be higher than in the project-specific analysis, resulting in an elevated potential of fault reactivation. The tool allows a higher temperature differential for the reservoir conditions, especially the higher depth. The temperature differential where this case does not exceed SCU > 1.0 is 54°C. Note that this is already significantly higher than the temperature differential in the Centraal Nederland case as the higher depth and thickness allows for a higher temperature differential.

Depth (m)	2450
Reservoir thickness (m)	200
Offset fault (m) (positive for "normal" fault, negative for "reverse" fault)	30
(Reservoir T minus injection T) (°C)	58
(Injector FBHP - Reservoir pressure) (bar)	6
Distance injector - fault (m)	200
Closest distance cold front - fault (m)	0
Result of screening calculations	
There is **ELEVATED** risk of fault reactivation	
SCU (conservative upper limit)	**1.000**
Temperature contribution	99%
Pressure contribution	1%

Figure 4-3 The tool applied to the Noord-Holland case

4.5 REMARKS

The above cases highlight the importance of a location-specific analysis if a risk is deemed high enough to have cause of concern. Later analysis can make use of the specific conditions in depth and include probabilistic methods to address the uncertainty of these conditions. Especially higher temperature differentials can prove to have higher potential of fault reactivation and would sooner warrant a more detailed analysis. The impact of a differing temperature differential is captured in the screening tool.

5 Conclusion

The results of this study were used to compile type curves for fault reactivation under operating conditions ΔT and ΔP. The type curves are integrated in the accompanied tool and discern projects which have a *low* potential of fault reactivation versus an *elevated* potential of fault reactivation. The input for the type curves is deliberately conservative in terms of fault properties and stress field. The case studies highlight the importance of a location-specific analysis if the potential of fault reactivation is deemed high enough to have cause of concern. In the case of an elevated potential, it is suggested to be followed up by a site-specific analysis including parameters, uncertainties and a Monte Carlo simulation. This can be part of the future locationpecific evaluation. The input for the type curves is deliberately conservative in terms of fault properties and stress field. If new data would be available that warrants a change in any of the above parameters this can be changed directly in the tool without impacting the results from the type curve study.

6 References

Goodier, J.N. 1937. *On the Integration of the thermoelastic equations.* . Phil. Mag. Ser. 7, Vol. 23, pp. 1017-1032.

IF Technology & Q-con. 2016. „Defining the Framework for Seismic Hazard Assessment in Geothermal Projects 5 V0.1."

Koning, E.J.L. 1988. Waterflooding under fracturing conditions. PhD Thesis, Technical University of Delft, Chapter 3.

Lehner, F.K. 2019. „An analysis of depletion-induced fault stressing." Report SR..19.01549, Shell Global Solutions International B.V. https://nam-onderzoeksrapporten.data-app.nl/reports/download/groningen/en/147f324f-96be-4d88-a240-c14d6828ea47.

Nowacki, W. 1986. *Thermoelasticity, 2nd Edition.* . PWN – Polish Scientific Publishers, Warsaw, Pergamon Press, Oxford, pp. 539.

TNO. 2015. „Integrated pressure information system for the onshore and offshore Netherlands. Final Report R10056."

van den Bogert, P.A.J. 2019. „An analytical approach to fault rupturing in depleting gas reservoirs With application to the Groningen field, The Netherlands,." *Third Schatzalp Workshop on Induced Seismicity.* Davos: DOI: 10.13140/RG.2.2.34418.15.

van den Bogert, P.A.J., en R.M.H.E. van Eijs. 2020. *Why Mohr-circle analyses may underestimate the risk of fault reactivation in depleting reservoirs.* International Journal of Rock Mechanics and Mining Sciences 136: 104502.

van den Hoek, Paul, en Jorik Poessé. 2021. „Assessment of seismic risk in geothermal and hydrocarbon reservoirs using an exact analytical solution of stress change.", SPE-205122 , presented at the SPE Europec featured at the 83rd EAGE Conference and Exhibition held in Amsterdam, October.

Verweij, J.M., H.J. Simmelink, J. Underschultz, en J. Witmans. 2012. *Pressure and fluid dynamic characterisation of the Dutch subsurface.* Netherlands Journal of Geosciences, 91-4, p. 465-490.

Appendix A Type curves for dimensionless stress change by temperature

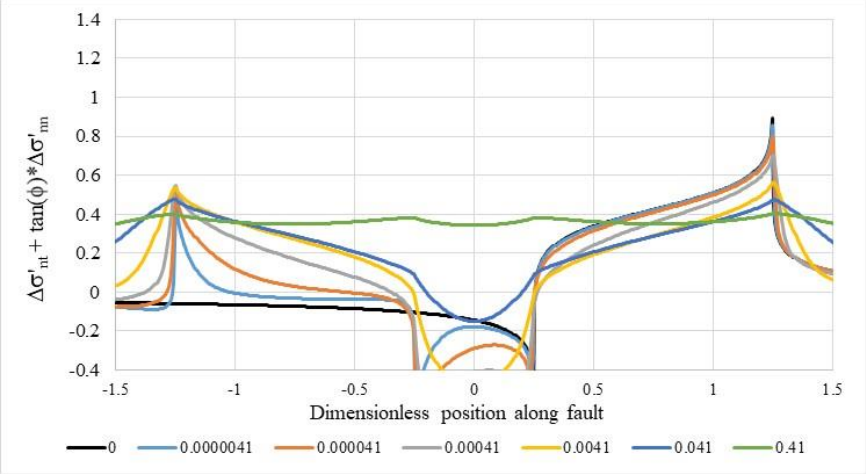

Fig. A1. Type curves of $\Delta\sigma'_{ntD} + tan(\varphi).\Delta\sigma'_{nnD}$ for a range of dimensionless times t_D after crossing the fault, and for dimensionless offset −1.5.

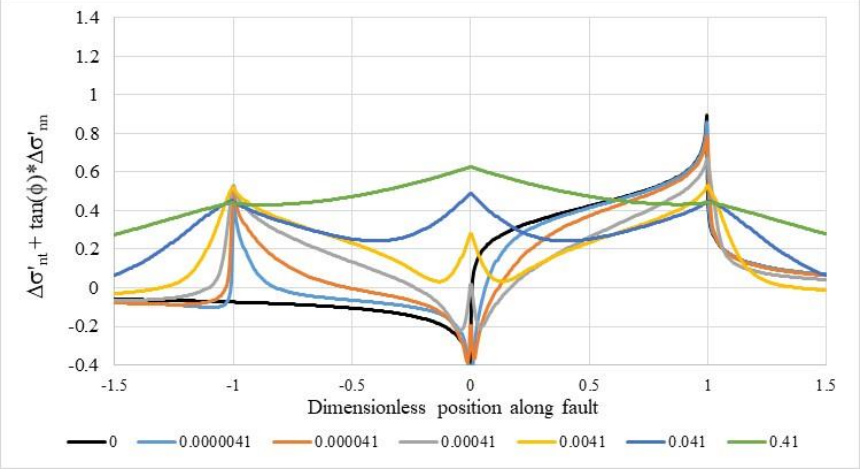

Fig. A2. Type curves of $\Delta\sigma'_{ntD} + tan(\varphi).\Delta\sigma'_{nnD}$ for a range of dimensionless times t_D after crossing the fault, and for dimensionless offset −1.0.

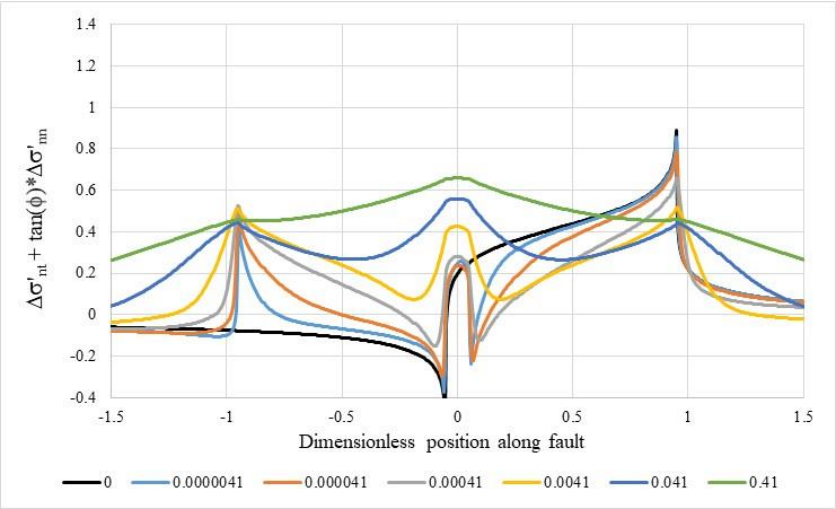

Fig. A3. Type curves of $\Delta\sigma'_{ntD} + tan(\varphi).\Delta\sigma'_{nnD}$ for a range of dimensionless times t_D after crossing the fault, and for dimensionless offset –0.9.

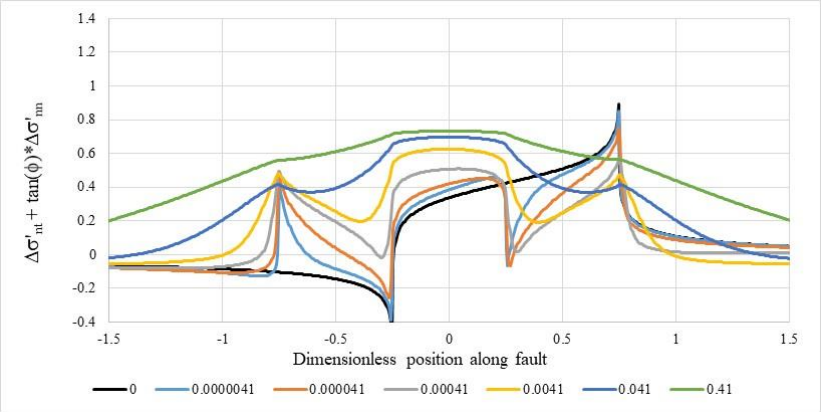

Fig. A4. Type curves of $\Delta\sigma'_{ntD} + tan(\varphi).\Delta\sigma'_{nnD}$ for a range of dimensionless times t_D after crossing the fault, and for dimensionless offset –0.5.

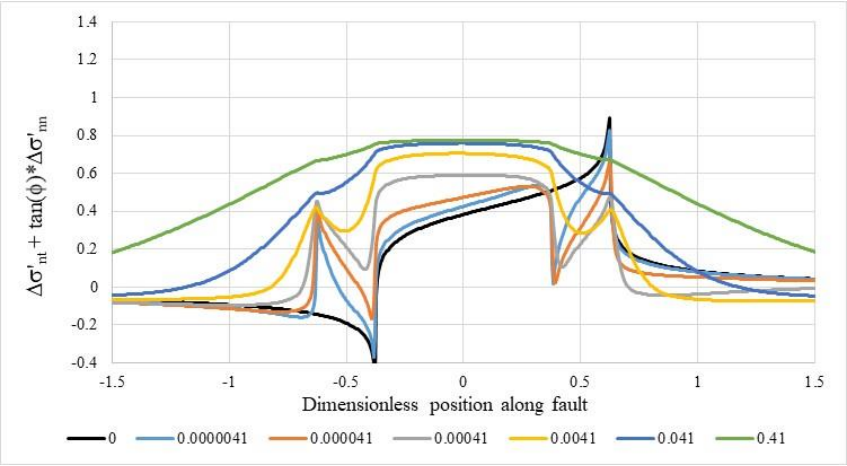

Fig. A5. Type curves of $\Delta\sigma'_{ntD} + tan(\varphi).\Delta\sigma'_{nnD}$ for a range of dimensionless times t_D after crossing the fault, and for dimensionless offset –0.25.

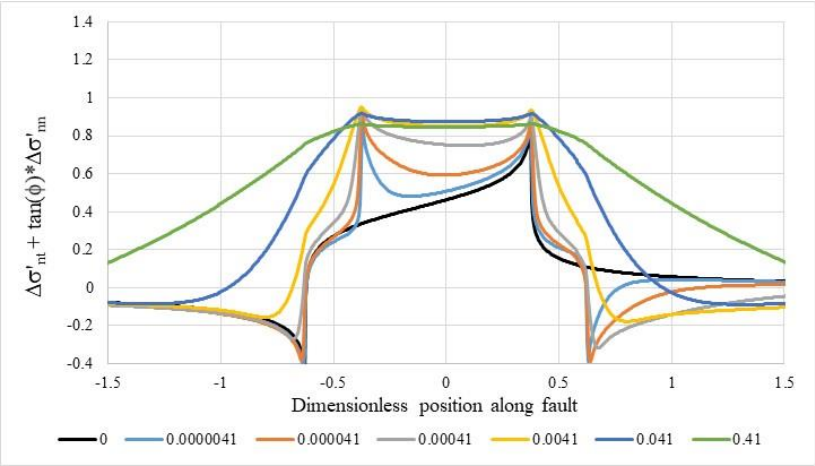

Fig. A6. Type curves of $\Delta\sigma'_{ntD} + tan(\varphi).\Delta\sigma'_{nnD}$ for a range of dimensionless times t_D after crossing the fault, and for dimensionless offset +0.25.

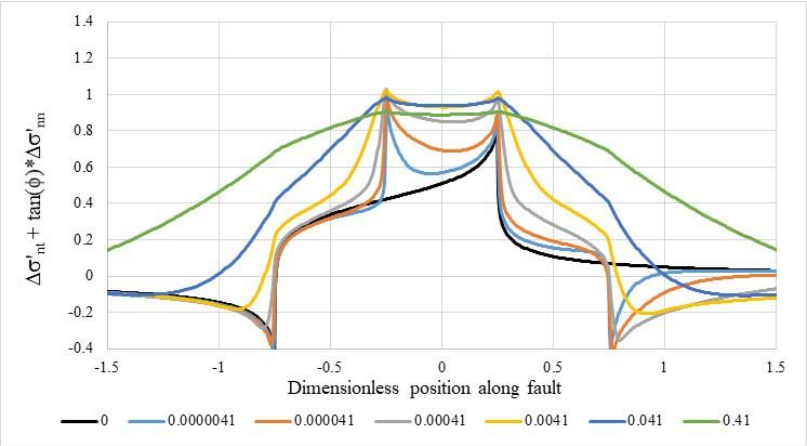

Fig. A7. Type curves of $\Delta\sigma'_{ntD} + tan(\varphi).\Delta\sigma'_{nnD}$ for a range of dimensionless times t_D after crossing the fault, and for dimensionless offset +0.5.

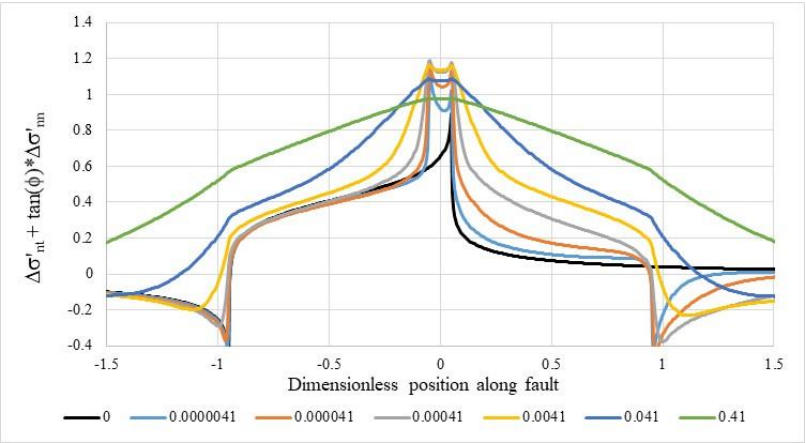

Fig. A8. Type curves of $\Delta\sigma'_{ntD} + tan(\varphi).\Delta\sigma'_{nnD}$ for a range of dimensionless times t_D after crossing the fault, and for dimensionless offset +0.9.

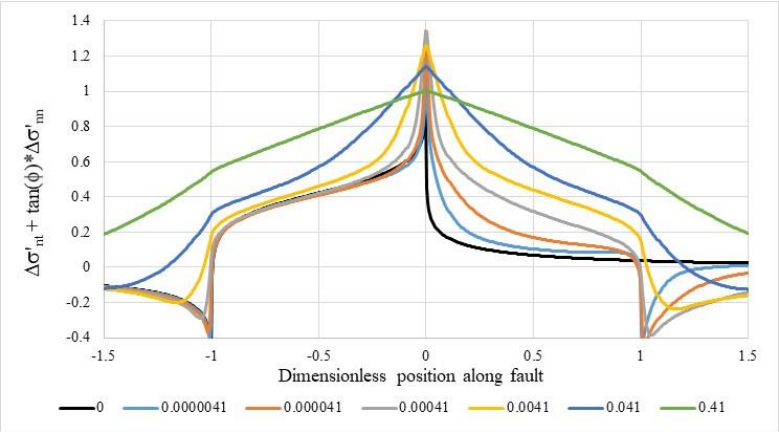

Fig. A9. Type curves of $\Delta\sigma'_{ntD} + tan(\varphi).\Delta\sigma'_{nnD}$ for a range of dimensionless times t_D after crossing the fault, and for dimensionless offset +1.0.

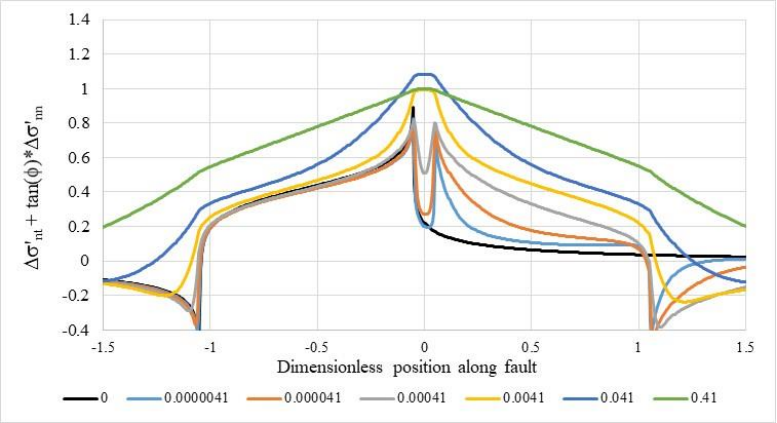

Fig. A10. Type curves of $\Delta\sigma'_{ntD} + tan(\varphi).\Delta\sigma'_{nnD}$ for a range of dimensionless times t_D after crossing the fault, and for dimensionless offset +1.1.

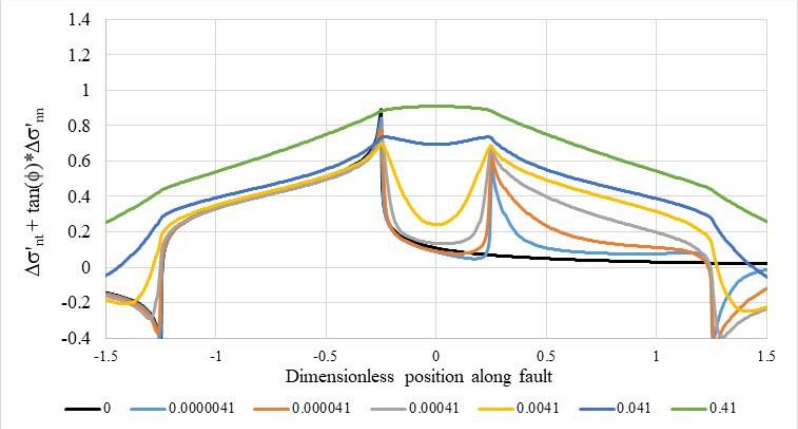

Fig. A11. Type curves of $\Delta\sigma'_{ntD} + tan(\varphi).\Delta\sigma'_{nnD}$ for a range of dimensionless times t_D after crossing the fault, and for dimensionless offset +1.5.

Appendix B Type curves for dimensionless stress change by pressure

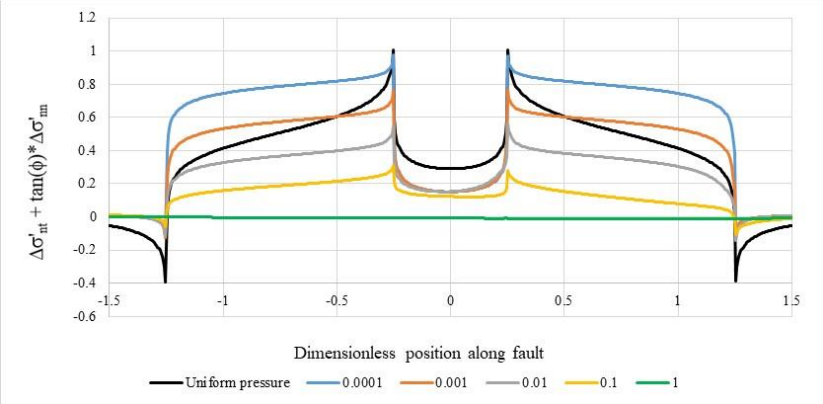

Fig. B1. Type curves of $\Delta\sigma'_{ntD} + tan(\varphi).\Delta\sigma'_{nnD}$ for a range of dimensionless distances d/R_e between injector and fault, and for dimensionless offset −1.5. For comparison, also the case of uniform pressure increase equal to the injector pressure increase is given (black curve).

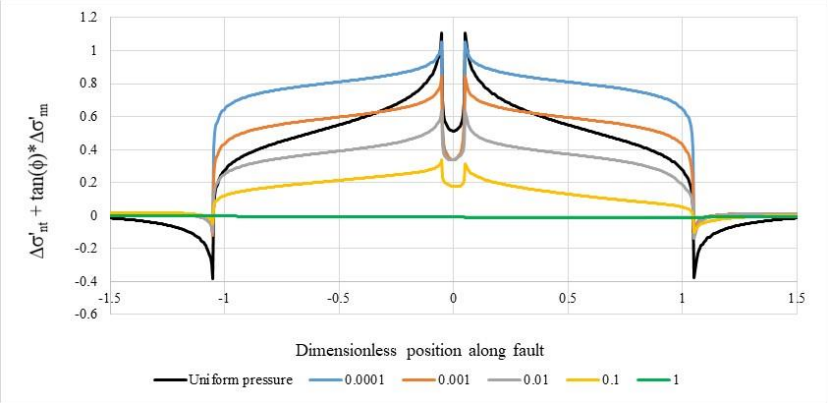

Fig. B2. Type curves of $\Delta\sigma'_{ntD} + tan(\varphi).\Delta\sigma'_{nnD}$ for a range of dimensionless distances d/R_e between injector and fault, and for dimensionless offset −1.1. For comparison, also the case of uniform pressure increase equal to the injector pessure increase is given (black curve).

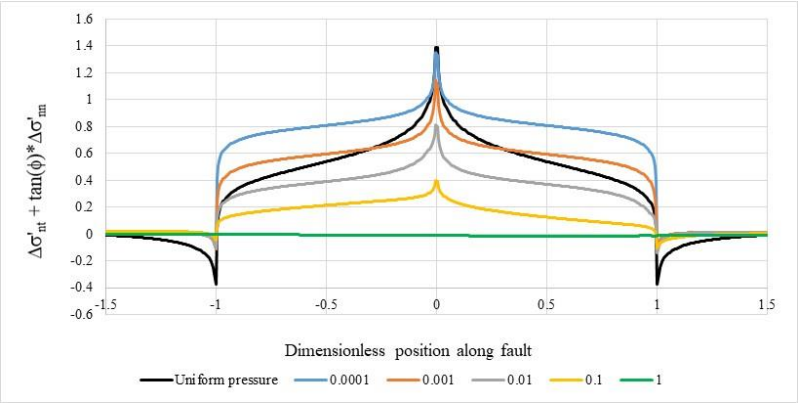

Fig. B3. Type curves of $\Delta\sigma'_{ntD} + tan(\varphi).\Delta\sigma'_{nnD}$ for a range of dimensionless distances d/R_e between injector and fault, and for dimensionless offset –1.0. For comparison, also the case of uniform pressure increase equal to the injector pressure increase is given (black curve).

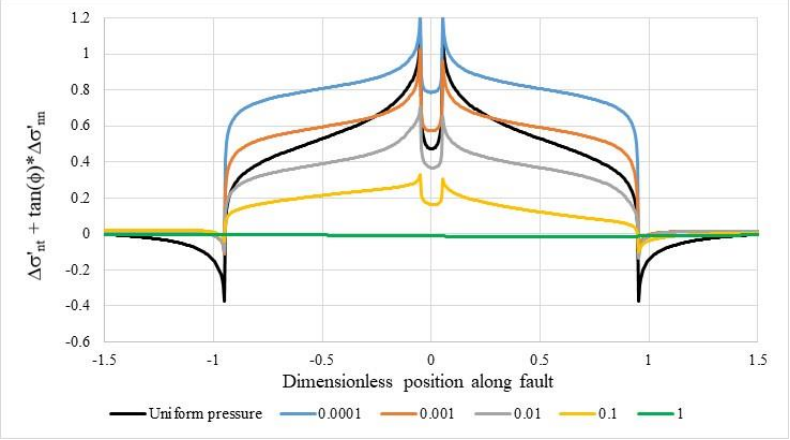

Fig. B4. Type curves of $\Delta\sigma'_{ntD} + tan(\varphi).\Delta\sigma'_{nnD}$ for a range of dimensionless distances d/R_e between injector and fault, and for dimensionless offset –0.9. For comparison, also the case of uniform pressure increase equal to the injector pressure increase is given (black curve).

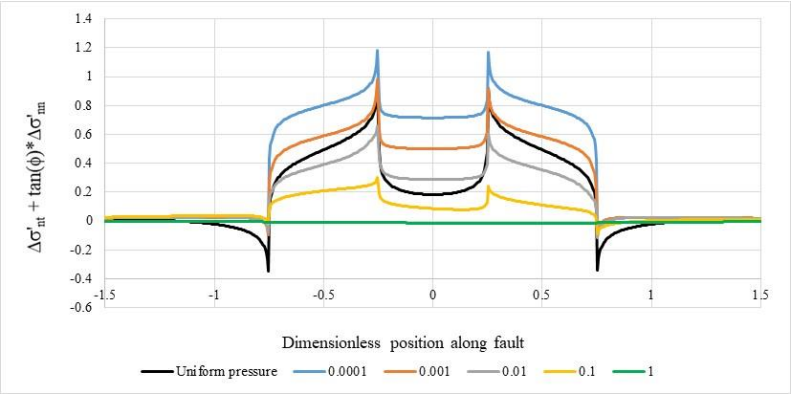

Fig. B5. Type curves of $\Delta\sigma'_{ntD} + tan(\varphi).\Delta\sigma'_{nnD}$ for a range of dimensionless distances d/R_e between injector and fault, and for dimensionless offset –0.5. For comparison, also the case of uniform pressure increase equal to the injector pressure increase is given (black curve).

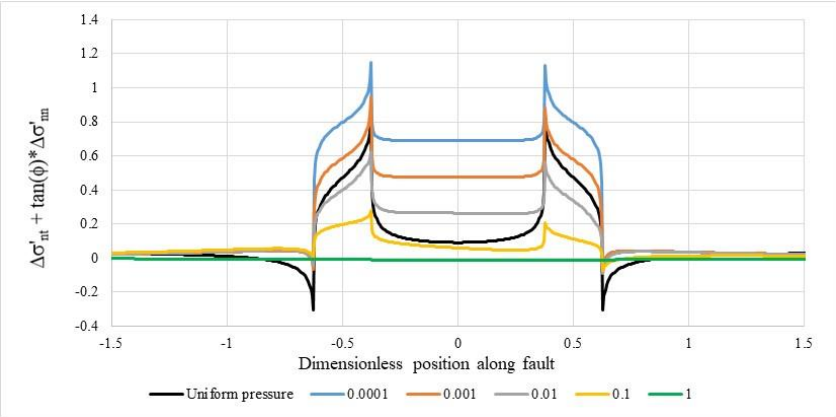

Fig. B6. Type curves of $\Delta\sigma'_{ntD} + tan(\varphi).\Delta\sigma'_{nnD}$ for a range of dimensionless distances d/R_e between injector and fault, and for dimensionless offset –0.25. For comparison, also the case of uniform pressure increase equal to the injector pressure increase is given (black curve).

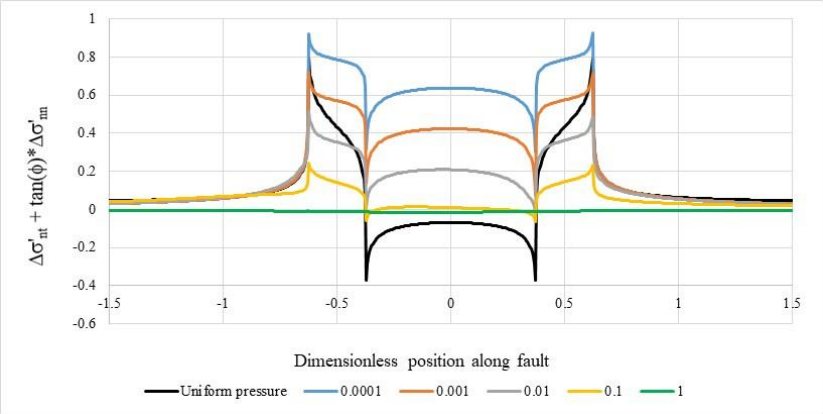

Fig. B7. Type curves of $\Delta\sigma'_{ntD} + tan(\varphi).\Delta\sigma'_{nnD}$ for a range of dimensionless distances d/R_e between injector and fault, and for dimensionless offset +0.25. For comparison, also the case of uniform pressure increase equal to the injector pressure increase is given (black curve).

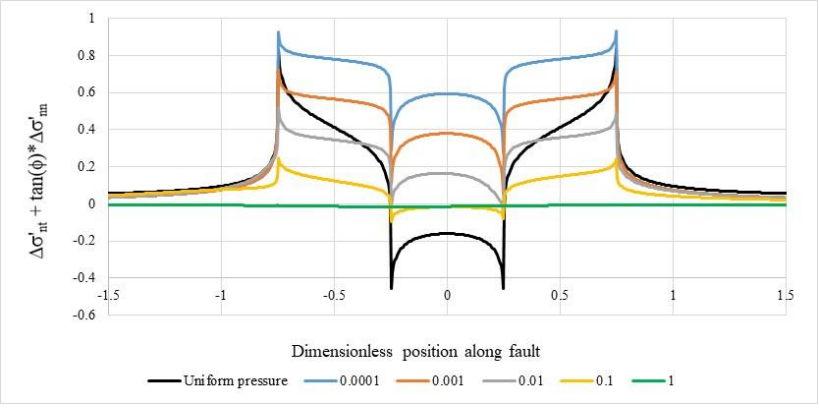

Fig. B8. Type curves of $\Delta\sigma'_{ntD} + tan(\varphi).\Delta\sigma'_{nnD}$ for a range of dimensionless distances d/R_e between injector and fault, and for dimensionless offset +0.5. For comparison, also the case of uniform pressure increase equal to the injector pressure increase is given (black curve).

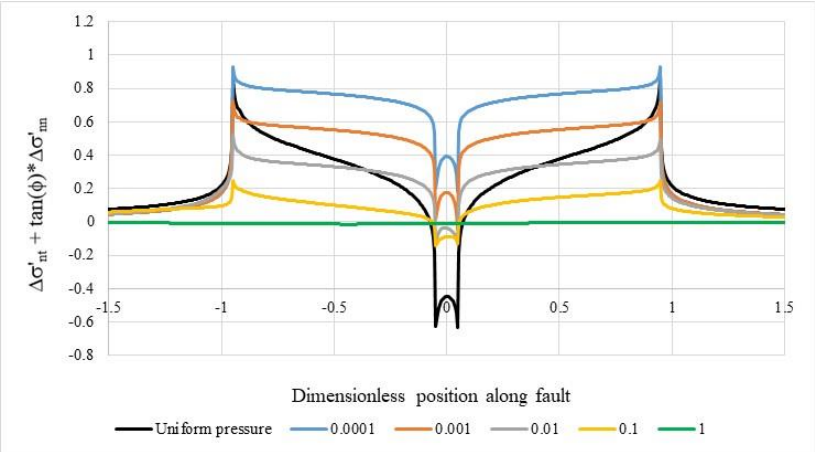

Fig. B9. Type curves of $\Delta\sigma'_{ntD} + tan(\varphi).\Delta\sigma'_{nnD}$ for a range of dimensionless distances d/R_e between injector and fault, and for dimensionless offset +0.9. For comparison, also the case of uniform pressure increase equal to the injector pessure increase is given (black curve).

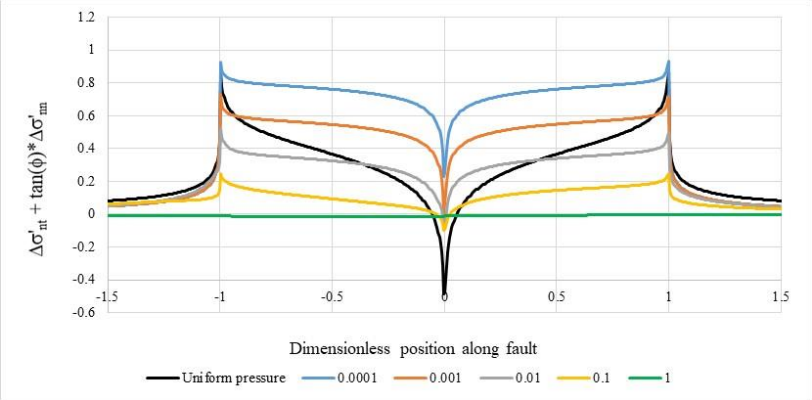

Fig. B10. Type curves of $\Delta\sigma'_{ntD} + tan(\varphi).\Delta\sigma'_{nnD}$ for a range of dimensionless distances d/R_e between injector and fault, and for dimensionless offset +1.0. For comparison, also the case of uniform pressure increase equal to the injector pressure increase is given (black curve).

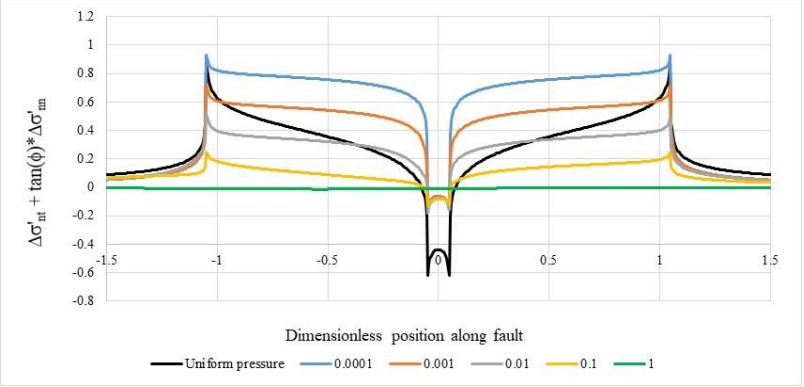

Fig. B11. Type curves of $\Delta\sigma'_{ntD} + tan(\varphi).\Delta\sigma'_{nnD}$ for a range of dimensionless distances d/R_e between injector and fault, and for dimensionless offset +1.1. For comparison, also the case of uniform pressure increase equal to the injector pressure increase is given (black curve).

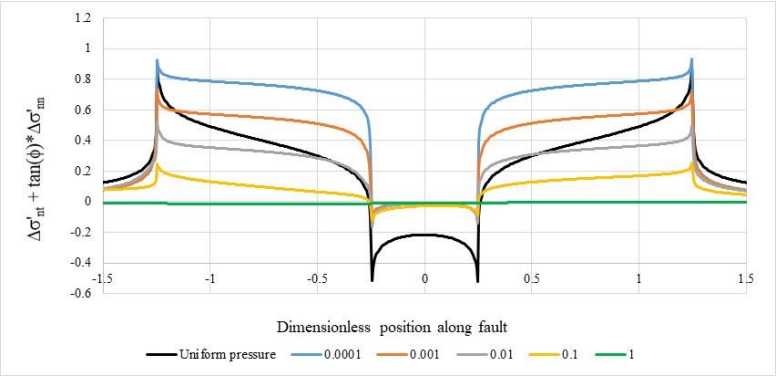

Fig. B12. Type curves of $\Delta\sigma'_{ntD} + tan(\varphi) . \Delta\sigma'_{nnD}$ for a range of dimensionless distances d/R_e between injector and fault, and for dimensionless offset +1.5. For comparison, also the case of uniform pressure increase equal to the injector pressure increase is given (black curve).